RESEARCH ARTICLE SUMMARY

PROTEIN DESIGN

Designed proteins assemble antibodies into modular nanocages

Robby Divine, Ha V. Dang, George Ueda, Jorge A. Fallas, Ivan Vulovic, William Sheffler, Shally Saini, Yan Ting Zhao, Infencia Xavier Raj, Peter A. Morawski, Madeleine F. Jennewein, Leah J. Homad, Yu-Hsin Wan, Marti R. Tooley, Franziska Seeger, Ali Etemadi, Mitchell L. Fahning, James Lazarovits, Alex Roederer, Alexandra C. Walls, Lance Stewart, Mohammadali Mazloomi, Neil P. King, Daniel J. Campbell, Andrew T. McGuire, Leonidas Stamatatos, Hannele Ruohola-Baker, Julie Mathieu, David Veesler, David Baker*

INTRODUCTION: Antibodies that bind tightly to targets of interest play central roles in biological research and medicine. Clusters of antibodies, typically generated by fusing antibodies to polymers or genetically linking antibody fragments together, can enhance signaling. Currently lacking are approaches for making antibody assemblies with a range of precisely specified architectures and valencies.

RATIONALE: We set out to computationally design proteins that assemble antibodies into precise architectures with different valencies and symmetries. We developed an approach to designing proteins that position antibodies or Fc-fusions on the twofold symmetry axes of regular dihedral and polyhedral architectures. We hypothesized that such designs could robustly drive arbitrary antibodies into homogeneous and structurally well-defined nanocages and that such assemblies could have pronounced effects on cell signaling.

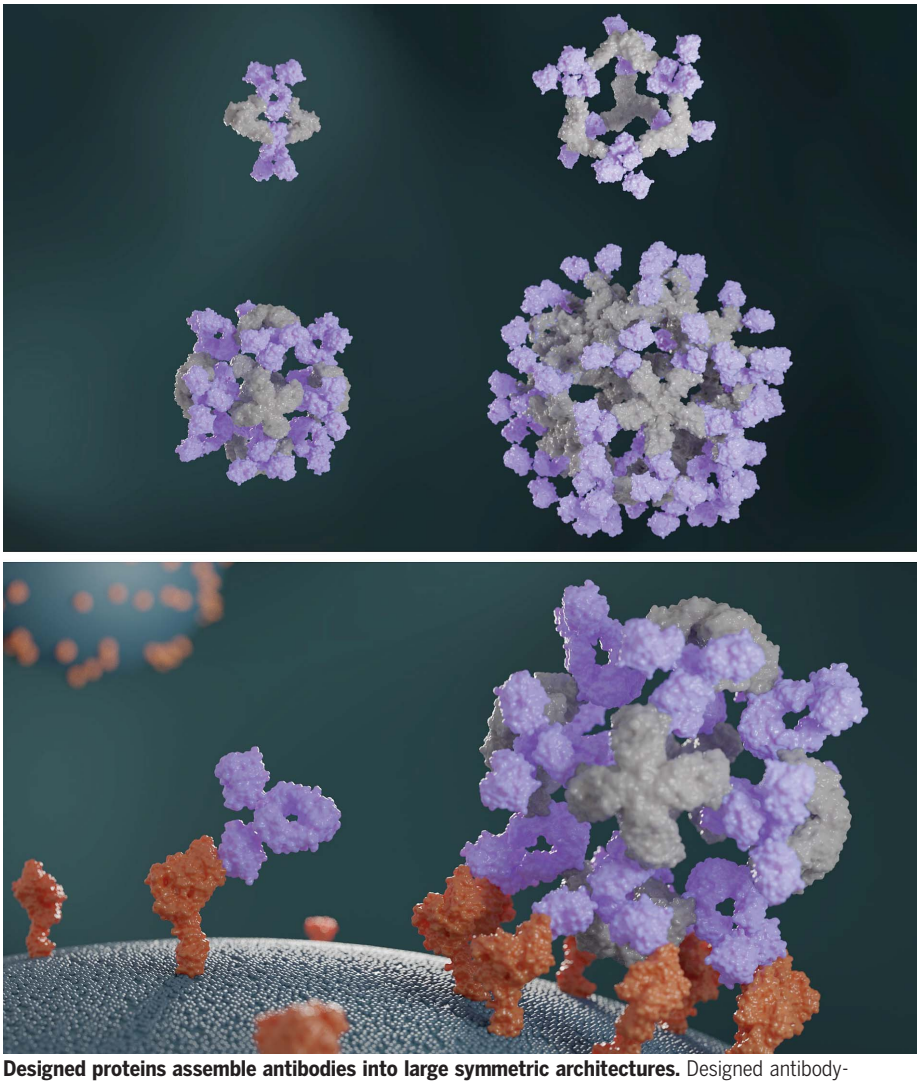

IMAGE: IAN HAYDON, INSTITUTE FOR PROTEIN DESIGN

Designed proteins assemble antibodies into large symmetric architectures. Designed antibody-clustering proteins (light gray) assemble antibodies (purple) into diverse nanocage architectures (top). Antibody nanocages enhance cell signaling compared with free antibodies (bottom).

RESULTS: Antibody cage (AbC)–forming designs were created by rigidly fusing antibody constant domain–binding modules to cyclic oligomers through helical spacer domains such that the symmetry axes of the dimeric antibody and cyclic oligomer are at orientations that generate different dihedral or polyhedral (e.g., tetrahedral, octahedral, or icosahedral) architectures. The junction regions between the connected building blocks were optimized to fold to the designed structures. Synthetic genes encoding the designs were expressed in bacterial cultures; of 48 structurally characterized designs, eight assemblies matched the design models. Successful designs encompass D2 dihedral (three designs), T32 tetrahedral (two designs), O42 octahedral (one design), and I52 icosahedral (two designs) architectures; these contain 2, 6, 12, or 30 antibodies, respectively.

We investigated the effects of AbCs on cell signaling. AbCs formed with a death receptor–targeting antibody induced apoptosis of tumor cell lines that were unaffected by the soluble antibody or the native ligand. Angiopoietin pathway signaling, CD40 signaling, and T cell proliferation were all enhanced by assembling Fc-fusions or antibodies in AbCs. AbC formation also enhanced in vitro viral neutralization of a severe acute respiratory syndrome coronavirus 2 pseudovirus.

CONCLUSION: We have designed multiple antibody cage–forming proteins that precisely cluster any protein A–binding antibody into nanocages with controlled valency and geometry. AbCs can be formed with 2, 6, 12, or 30 antibodies simply by mixing the antibody with the corresponding designed protein, without the need for any covalent modification of the antibody. Incorporating receptor binding or virus-neutralizing antibodies into AbCs enhanced their biological activity across a range of cell systems. We expect that our rapid and robust approach for assembling antibodies into homogeneous and ordered nanocages without the need for covalent modification will have broad utility in research and medicine. ■

The list of author affiliations is available in the full article online.
*Corresponding author. Email: dabaker@uw.edu
Cite this article as R. Divine *et al.*, *Science* **372**, eabd9994 (2021). DOI: 10.1126/science.abd9994

READ THE FULL ARTICLE AT
https://doi.org/10.1126/science.abd9994

RESEARCH ARTICLE

PROTEIN DESIGN

Designed proteins assemble antibodies into modular nanocages

Robby Divine[1,2], Ha V. Dang[1], George Ueda[1,2], Jorge A. Fallas[1,2], Ivan Vulovic[1,2], William Sheffler[2], Shally Saini[1,3], Yan Ting Zhao[1,3,4], Infencia Xavier Raj[1,3], Peter A. Morawski[5], Madeleine F. Jennewein[6], Leah J. Homad[6], Yu-Hsin Wan[6], Marti R. Tooley[2], Franziska Seeger[1,2], Ali Etemadi[2,7], Mitchell L. Fahning[5], James Lazarovits[1,2], Alex Roederer[2], Alexandra C. Walls[1], Lance Stewart[2], Mohammadali Mazloomi[7], Neil P. King[1,2], Daniel J. Campbell[5], Andrew T. McGuire[6,8], Leonidas Stamatatos[6,8], Hannele Ruohola-Baker[1,3], Julie Mathieu[3,9], David Veesler[1], David Baker[1,2,10]*

Multivalent display of receptor-engaging antibodies or ligands can enhance their activity. Instead of achieving multivalency by attachment to preexisting scaffolds, here we unite form and function by the computational design of nanocages in which one structural component is an antibody or Fc-ligand fusion and the second is a designed antibody-binding homo-oligomer that drives nanocage assembly. Structures of eight nanocages determined by electron microscopy spanning dihedral, tetrahedral, octahedral, and icosahedral architectures with 2, 6, 12, and 30 antibodies per nanocage, respectively, closely match the corresponding computational models. Antibody nanocages targeting cell surface receptors enhance signaling compared with free antibodies or Fc-fusions in death receptor 5 (DR5)–mediated apoptosis, angiopoietin-1 receptor (Tie2)–mediated angiogenesis, CD40 activation, and T cell proliferation. Nanocage assembly also increases severe acute respiratory syndrome coronavirus 2 (SARS-CoV-2) pseudovirus neutralization by α-SARS-CoV-2 monoclonal antibodies and Fc–angiotensin-converting enzyme 2 (ACE2) fusion proteins.

Antibodies that bind with high specificity and affinity to targets of interest are widely used as therapeutics and biological research tools. (*1*). For the purposes of increasing binding avidity and enhancing agonism through receptor clustering, high-valency antibody formats that present more than two antigen-binding sites have been explored. (*2*, *3*). Current techniques for creating multivalent antibody-presenting formats include chaining together multiple antigen-binding fragments (*4*, *5*), pentameric immunoglobulin M (IgM) or IgM derivatives such as Fc domain hexamers (*6*), dimeric immunoglobulin G (IgG) attachment to inorganic materials (*7*), or protein oligomers or nanoparticles (*8*–*13*). These approaches often require extensive engineering or multiple-step conjugation reactions for each desired antibody oligomer. In the case of nanoparticles with flexibly linked IgG-binding domains, it is difficult to ensure full IgG occupancy on the particle surface and to prevent particle flocculation, which is induced when multiple nanoparticles bind to dimeric IgGs. Methods for creating antibody-based protein nanoparticles across multiple valencies with precisely controlled geometry and composition that are applicable to the many available IgG antibodies could have very broad utility.

A general computational method for antibody cage design

We sought to design proteins that drive the assembly of arbitrary antibodies into symmetric assemblies with well-defined structures. Previous design efforts built nanocages by computationally fusing (*14*, *15*) or docking together (*16*, *17*) protein building blocks with cyclic symmetry so that the symmetry axes of the building blocks align with those of a target architecture. For example, an I52 icosahedral assembly is built by bringing together a pentamer and a dimer that align to the icosahedral five- and twofold symmetry axes. We reasoned that symmetric protein assemblies could be built directly from IgG antibodies, which are twofold symmetric proteins, by designing cyclic oligomers that bind the IgG such that the symmetry axes of the antibody and the designed oligomer generate a desired target nanocage architecture. We designed such proteins by rigidly fusing together three types of "building block" units: antibody Fc-binding domains, helical repeat connectors, and cyclic oligomer–forming modules. The Fc-binding unit binds and positions the C2 antibody dimer, the cyclic homo-oligomer forms the second cyclic symmetry axis in the nanocage, and the helical repeat connector links the antibody and cyclic homo-oligomer symmetry axes together in the correct orientation to form the antibody nanocages (hereafter, AbCs, for antibody cages).

Large sets of building blocks with many possible fusion sites per building block are key to the success of this fusion approach, as rather-stringent geometric criteria must be met to precisely orient the symmetry axes of the antibody and cyclic oligomer to form the desired symmetric architecture. We used protein A (*18*), which recognizes the Fc domain of the IgG constant region, as one of two antibody-binding building blocks and designed a second Fc-binding building block by grafting the protein A interface residues onto a previously designed helical repeat protein (fig. S1) (*18*, *19*). Our final library consisted of these two Fc-binding proteins (*18*), 42 de novo designed helical repeat protein connectors (*19*), and between one and three designed cyclic homo-oligomers depending on geometry (two C2s, three C3s, one C4, and one C5) (*20*, *21*). An average of roughly 150 residues were available for fusion per protein building block, avoiding all positions at the Fc or homo-oligomer protein interface, leading to on the order of 10^7 possible tripartite (i.e., Fc-binder–connector–homo-oligomer) fusions. For each of these tripartite fusions, the rigid body transform between the internal homo-oligomeric interface and the Fc-binding interface is determined by the shapes of each of its three building blocks and the locations and geometry of the "junctions" that link them into a single subunit.

We used a computational protocol that rapidly samples all tripartite possible fusions from our building block library to identify those with the net rigid body transforms required to generate dihedral, tetrahedral, octahedral, and icosahedral AbCs (*14*, *15*). To describe the final nanocage architectures, we follow a naming convention that summarizes the point group symmetry and the cyclic symmetries of the building blocks (*16*). For example, a T32 assembly has tetrahedral point group symmetry and is built out of a C3 cyclic symmetric antibody-binding designed oligomer and the C2 cyclic symmetric antibody Fc. While the antibody dimer aligns along the twofold axis in all architectures, the designed component is a second homodimer in D2 dihedral structures; a homotrimer in T32 tetrahedral structures, O32 octahedral structures, and I32 icosahedral structures; a homotetramer in O42

[1]Department of Biochemistry, University of Washington, Seattle, WA 98195, USA. [2]Institute for Protein Design, University of Washington, Seattle, WA 98195, USA. [3]Institute for Stem Cell and Regenerative Medicine, University of Washington, Seattle, WA 98109, USA. [4]Oral Health Sciences, School of Dentistry, University of Washington, Seattle, WA 98195, USA. [5]Benaroya Research Institute, Seattle, WA 98101, USA. [6]Vaccines and Infectious Disease Division, Fred Hutchinson Cancer Research Center, Seattle, WA 98019, USA. [7]Medical Biotechnology Department, School of Advanced Technologies in Medicine, Tehran University of Medical Sciences (TUMS), Tehran, Iran. [8]Department of Global Health, University of Washington, Seattle, WA 98195, USA. [9]Department of Comparative Medicine, University of Washington, Seattle, WA 98195, USA. [10]Howard Hughes Medical Institute, University of Washington, Seattle, WA 98195, USA.
*Corresponding author. Email: dabaker@uw.edu

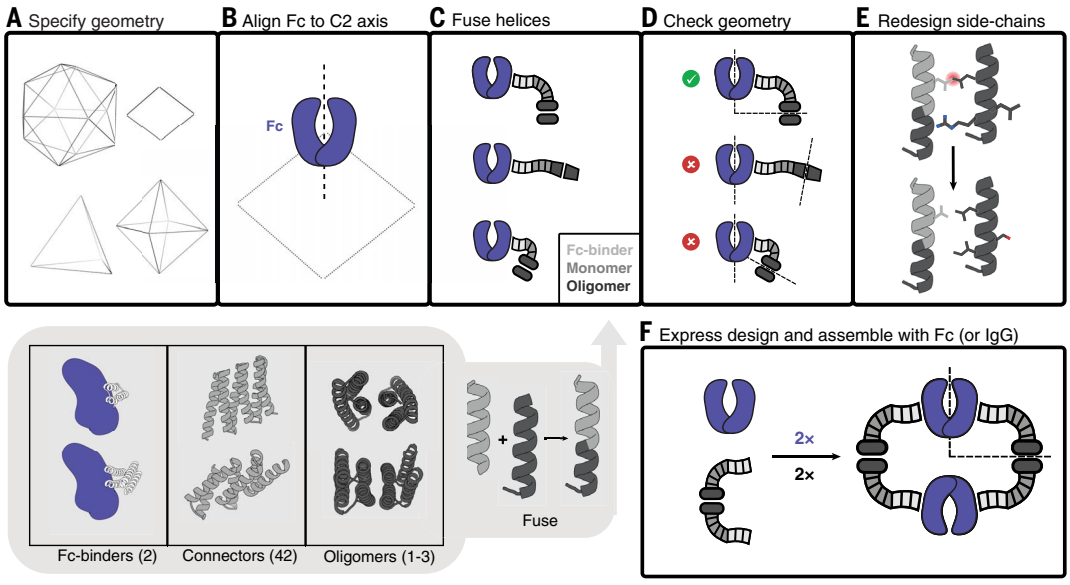

Fig. 1. Antibody nanocage (AbC) design. (**A**) Polyhedral geometry is specified. Clockwise from top left: icosahedral, dihedral, octahedral, and tetrahedral geometries are shown. (**B**) An antibody Fc model from hIgG1 is aligned to one of the C2 axes (in this case, a D2 dihedron is shown). (**C**) Antibody Fc-binders are fused to helical repeat connectors that are then fused to the monomeric subunit of helical cyclic oligomers. All combinations of building blocks and building block junctions are sampled (gray-shaded bottom inset; numbers in parentheses refer to the number of building blocks available). (**D**) Tripartite fusions are checked to ensure successful alignment of the C2 Fc symmetry axes with that of the polyhedral architecture (in the case of the D2 symmetry shown here, the C2 axes must intersect at a 90° angle). (**E**) Fusions that pass the geometric criteria move forward with side-chain redesign, where, for example, amino acids are optimized to ensure that core-packing residues are nonpolar and closely packed and that solvent-exposed residues are polar. (**F**) Designed AbC-forming oligomers are bacterially expressed, purified, and assembled with antibody Fc or IgG.

octahedral structures; and a homopentamer in I52 icosahedral structures.

To generate the fusions, the protocol first aligns the model of the Fc and Fc-binder protein along the C2 axis of the specified architecture (Fig. 1, A and B). The Fc-binder is then fused to a helical repeat connector, which is in turn fused to a homo-oligomer. Rigid helical fusions are made by superimposing residues in alpha helical secondary structure from each building block; in the resulting fused structure, one building block chain ends and the other begins at the fusion point, forming a new, continuous alpha helix (Fig. 1C). To drive formation of the desired nanocage architecture, helices are fused such that the antibody twofold axis and the symmetry axis of the homo-oligomer intersect at specified angles at the center of the architecture (Fig. 1D). To generate D2 dihedral, T32 tetrahedral, O32 or O42 octahedral, and I32 or I52 icosahedral nanocages, the required intersection angles are 90.0°, 54.7°, 35.3°, 45.0°, 20.9°, and 31.7°, respectively (*22*). We allowed angular and distance deviations from the ideal architecture of at most 5.7° and 0.5 Å, respectively (see the Materials and methods section). Candidate fusion models were further filtered on the basis of the number of contacts around the fusion junction (to gauge structural rigidity) and clashes between backbone atoms. Next, the amino acid identities and conformations around the newly formed building block junction were optimized using the SymPackRotamersMover in Rosetta to maintain the rigid fusion geometry required for assembly (Fig. 1, E and F). After sequence design, we selected for experimental characterization six D2 dihedral, eleven T32 tetrahedral, four O32 octahedral, two O42 octahedral, fourteen I32 icosahedral, and eleven I52 icosahedral designs predicted to form AbCs.

Structural characterization

Synthetic genes encoding designed protein sequences appended with a C-terminal 6×histidine tag were expressed in *Escherichia coli*. Designs were purified from clarified lysates using immobilized metal affinity chromatography (IMAC), and size exclusion chromatography (SEC) was used as a final purification step. Across all geometries, 34 of 48 AbC-forming designs had a peak on SEC that roughly corresponded to the expected size of the design model (fig. S2 and table S1). Designs were then combined with human IgG1 (hIgG1) Fc, and the assemblies were purified via SEC.

Eight of these AbC-forming designs readily self-assembled after mixing with Fc into a species that eluted as a monodisperse peak at a volume consistent with the target nanoparticle molecular size (Fig. 2, A and B; three D2 dihedral, two T32 tetrahedral, one O42 octahedral, and two I52 icosahedral AbCs). For the i52.6 design, adding 100 mM L-arginine to the assembly buffer prevented aggregation after combining with Fc (*23*); all other designs readily self-assembled in tris-buffered saline (TBS). Of these eight AbC-forming designs, all expressed well, with SEC-purified protein yields between 50 and 100 mg of protein per liter of bacterial culture. After combining with Fc, at least 90% of the protein injected on SEC is recovered in the assembly peak (Fig. 2B, leftmost peak). SEC peaks for the T32 and O42 designs were somewhat broader than other designs, spanning 3 to 4 ml in retention volume, as observed in previous nanocage design efforts (*16*). The I52 designs eluted in the void volume, consistent with their predicted diameters. Most other designs still bound Fc, as evidenced by SEC or by visibly precipitating with Fc after combination, but did not form monodisperse nanoparticles by SEC (table S1), perhaps because of deviations from the target fusion geometry.

We further characterized the eight Fc AbCs with monodisperse SEC profiles by small-angle x-ray scattering (SAXS) and electron microscopy (EM). SAXS spectra, pair distance distribution [$P(r)$], and radius of gyration (R_g) values were close to design models for d2.4, d2.7, t32.4, o42.1, i52.3, and i52.6 Fc AbCs (fig. S3 and table S2) (*24*, *25*). The agreement to the SAXS data for the d2.3 and t32.8 design models was somewhat poorer [higher R_g values and deviations in the SAXS Guinier (low-q) region and $P(r)$ distributions from those computed from the design model] potentially owing to alternate particle states, flexibility, and/or particle aggregation during data collection. Cryo-EM of o42.1 and i52.3 AbCs and negative stain EM (NS-EM) of the other six AbCs showed monodisperse particle formation with individual cages and two-dimensional (2D) class averages that resemble the design models (Fig. 2C and tables S3 and S4).

AbCs also formed when assembled with full IgG antibodies (containing both Fc and Fab domains), again generating monodisperse nanocages, as shown by SEC and NS-EM (Fig. 2, D and E); here, the o42.1 design with IgG

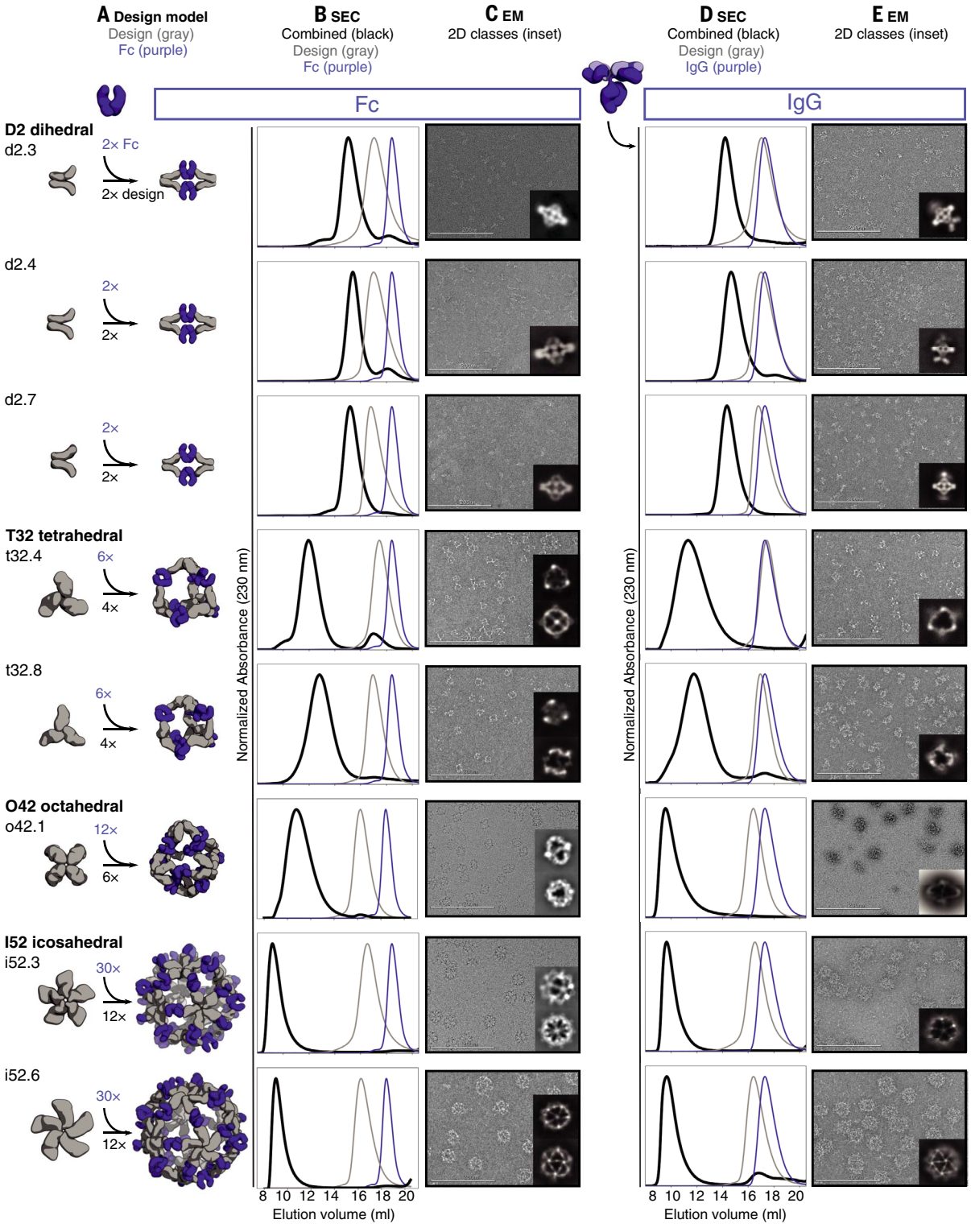

Fig. 2. Structural characterization of AbCs. (**A**) Design models, with antibody Fc (purple) and designed AbC-forming oligomers (gray). (**B**) Overlay of representative SEC traces of assembly formed by mixing design and Fc (black) with those of the single components in gray (design) or purple (Fc). (**C**) EM images with reference-free 2D class averages in inset; all data are from NS-EM, with the exception of designs o42.1 and i52.3 (cryo-EM). (**D** and **E**) SEC (D) and NS-EM representative micrographs with reference-free 2D class averages (E) of the same designed antibody cages assembled with full human IgG1 (with the 2 Fab regions intact). In all EM cases shown in (C) and (E), assemblies were first purified via SEC, and the fractions corresponding to the leftmost peak were pooled and used for imaging to remove any excess design or Ig component. Scale bars, 200 nm.

reproducibly elutes in the void owing to the increased diameter from the added Fab domains. There is considerably more evidence of flexibility in the electron micrographs of the IgG AbCs than the Fc AbCs, as expected given the flexibility of the Fc-Fab hinge. In all cases, 2D class averages obtained from the NS-EM data of AbCs made with intact IgG showed resolved density corresponding to the Fc and the design portion of the assembly (Fig. 2E).

Single-particle NS-EM and cryo-EM reconstructed 3D maps of the AbCs formed with Fc are in close agreement with the computational design models (Fig. 3). NS-EM reconstructions for the dihedral (d2.3, d2.4, and d2.7), tetrahedral (t32.4 and t32.8), and one of the icosahedral (i52.6) nanocages clearly show dimeric U-shaped Fcs and longer designed protein regions that fit together as computationally designed. A single-particle cryo-EM reconstruction for the o42.1 design with Fc has clear density for the six designed tetramers at the C4 vertices, which twist along the edges of the octahedral architecture to bind 12 dimeric Fcs, leaving the eight C3 faces unoccupied. The 3D density map for o42.1 with Fc suggests that the particle flexes outward compared with the design model, consistent with the SAXS R_g data. Cryo-EM density for i52.3 with Fc likewise recapitulates the 20-faced shape of a regular icosahedron, with 12 designed pentamers protruding at the C5 vertices (owing to the longer length of the C5 building block compared with the connector or Fc-binder), binding to 30 dimeric Fcs at the center of the edge, with 20 unoccupied C3 faces. Asymmetric cryo-EM reconstructions of o42.1 with Fc and i52.3 with Fc had similar overall features to their respective symmetrized maps (fig. S4).

In a second design round, we sought to design both the homo-oligomeric building block and the nanocage in one step, and we obtained AbCs with D3 symmetry, although the overall success rate was lower (fig. S5 and table S5). SEC of assembled Fc AbCs, SAXS analysis, NS-EM micrographs, 2D class averages, and 3D reconstructed maps are all consistent with the shape and size of the corresponding design models.

We next assessed the stability of AbCs. Dynamic light scattering (DLS) readings remained constant over a period of 4 weeks for all designs when incubated at room temperature, with the exception of i52.6, which showed some broadening of the hydrodynamic radius after 2 to 3 weeks (fig. S6 and table S6). Fc AbCs also did not show any degradation according to SDS–polyacrylamide gel electrophoresis (SDS-PAGE). We investigated whether AbCs formed with one Fc-fusion or IgG would exchange when incubated with excess Fc; this is relevant to future in vivo applications of the AbCs, where they would be in the presence of a high concentration of serum IgG. We formed o42.1 AbCs with green fluorescent protein (GFP)–Fc, then incubated these with 25-fold molar excess of red fluorescent protein (RFP)–Fc for up to 24 hours. SEC was used to separate the AbCs, and fluorescence readings were taken of the AbC peak fraction (fig. S7, A to C). Although the RFP-Fc signal increased slightly in the cage fraction (fig. S7, D and E, and table S7), the GFP-Fc signal was very close to that of the o42.1 GFP-Fc control, suggesting minimal exchange of the Fc-containing component out of the cage. Encouraged by these stability results, we moved forward with

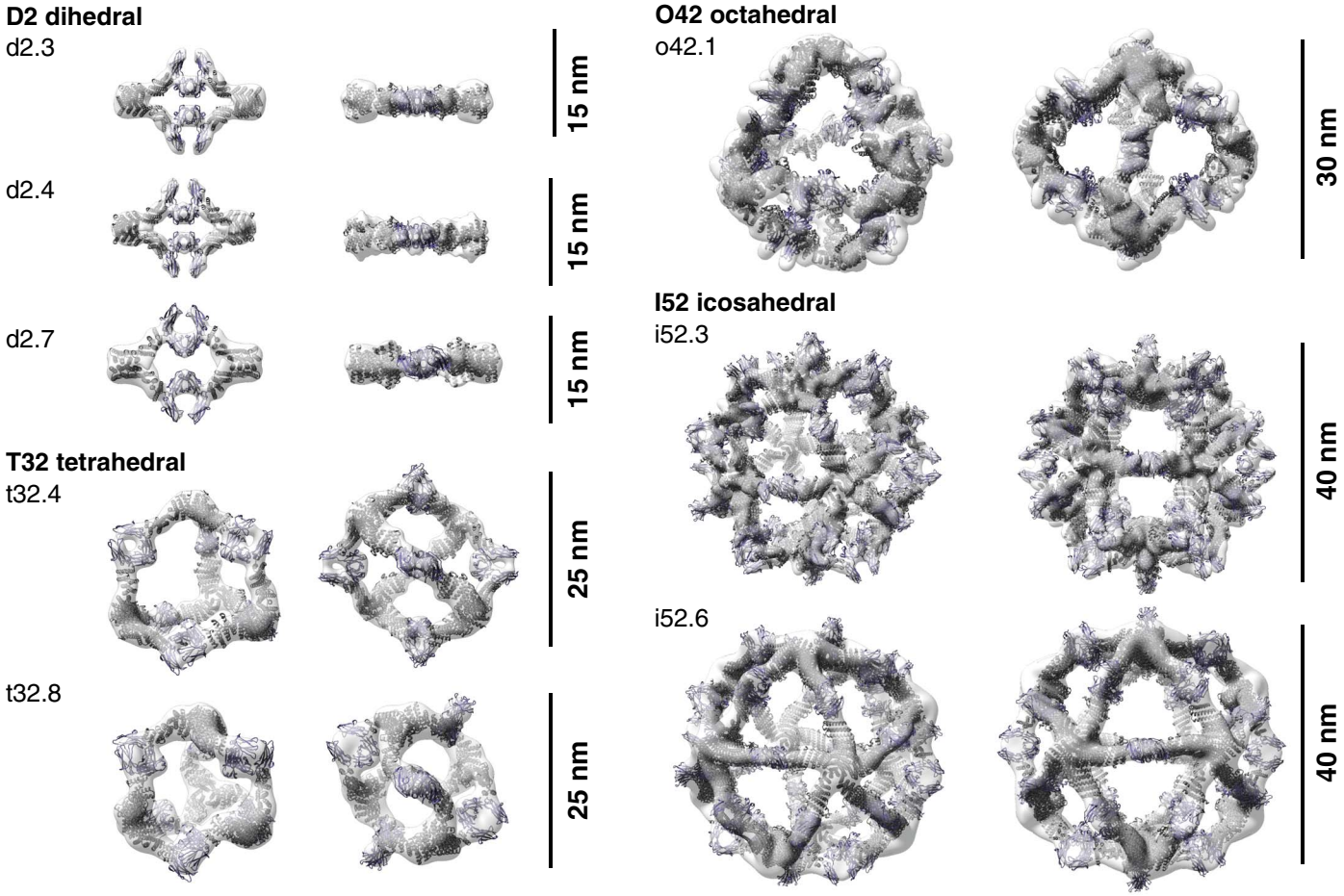

Fig. 3. 3D reconstructions of AbCs formed with Fc. Computational design models (cartoon representation) of each AbC are fit into the experimentally determined 3D density from EM. Each nanocage is viewed along an unoccupied symmetry axis (left) and rotated to look down one of the C2 axes of symmetry occupied by the Fc (right). Three-dimensional reconstructions from o42.1 and i52.3 are from cryo-EM analysis, all others are from NS-EM.

characterization of the biological impact of the AbCs.

Enhancing cell signaling with AbCs

Our designed AbCs provide a general platform for investigating the effect of valency and geometry of receptor engagement on signaling pathway activation. Receptor dimerization, trimerization, and higher-order association have been implicated in transmembrane signaling in different receptor systems, but systematically probing the influence on geometry and valency on signaling has required considerable system-specific engineering (*26*). The combination of the wide range of receptor binding antibodies and natural ligands with the AbC methodology developed here in principle allows ready and systematic probing of the effect of geometry and valency of receptor subunit association on signaling for almost any pathway.

To explore the potential of this approach, we assembled antibodies or Fc-ligand fusions targeting a variety of signaling pathways into nanocages and investigated their effects on signaling. We used multiple cage geometries in most applications; as the overall shapes of D2 dihedra were similar, only one D2 dihedral design was used, and design i52.6 was avoided because of the stability issues described above.

Induction of tumor cell apoptosis by α-DR5 nanocages

Death receptor 5 (DR5) is a tumor necrosis factor receptor (TNFR) superfamily cell surface protein that initiates a caspase-mediated apoptotic signaling cascade terminating in cell death when cross-linked by its trimeric native ligand, TNF-related apoptosis-inducing ligand (TRAIL) (*5*, *6*, *27*–*31*). Like other members of the family, DR5 can form alternative signaling complexes that activate nonapoptotic signaling pathways such as the nuclear factor κB proinflammatory pathway and pathways promoting proliferation and migration upon ligand binding (*30*). Because DR5 is overexpressed in some tumors, multiple therapeutic candidates have been developed to activate DR5, such as α-DR5 monoclonal antibodies and recombinant TRAIL, but these have failed in clinical trials owing to low efficacy and the development of TRAIL resistance in tumor cell populations (*30*, *31*). Combining trimeric TRAIL with bivalent α-DR5 IgG leads to a much stronger apoptotic response than either component by itself, likely because of induction of larger-scale DR5 clustering via the formation of 2D arrays on the cell surface (*28*).

We investigated whether α-DR5 AbCs formed with the same IgG (conatumumab) could have a similar antitumor effect without the formation of unbounded arrays. Five designs across four geometries were chosen (d2.4, t32.4, t32.8, o42.1, and i52.3) to represent the range of valencies and shapes (Fig. 4A). All α-DR5 AbCs were found to form single peaks on SEC, with corresponding NS-EM micrographs that were consistent with the formation of assembled particles (Fig. 2, D and E). All α-DR5 AbCs caused caspase-3 and -7 (caspase-3/7)–mediated apoptosis at similar levels to TRAIL in a colorectal tumor cell line (Colo205), whereas the antibody alone or AbCs formed with bare hIgG1 Fc did not lead to caspase-3/7 activity or cell death, even at the highest concentrations tested (comparing molarity on a per-antibody basis) (fig. S8A and table S8). In the TRAIL-resistant renal cell carcinoma line RCC4, we found that α-DR5 AbCs induced caspase-8 and caspase-3/7 activity (Fig. 4B and fig. S8, B and C) and designs t32.4, t32.8, and o42.1 greatly reduced cell viability at 150 nM concentration (Fig. 4C). Free α-DR5 antibody, Fc-only AbCs, or TRAIL neither activated caspase nor decreased cell viability after 4 days (Fig. 4, B to D, and fig. S8, B to D). Because designs t32.4 and o42.1 activated caspase-3/7 at less than one-hundredth of the concentration (1.5 nM) (Fig. 4B), we tested prolonged 6-day treatment of RCC4 cells with these AbCs at 150 nM. Nearly all cells were killed after 6 days, suggesting that RCC4 cells do not acquire resistance to the nanocages (Fig. 4E). We next investigated the downstream pathways activated by the α-DR5 AbCs by analyzing their effects on cleaved poly(ADP-ribose) polymerase (PARP), a measure of apoptotic activity. In agreement with the caspase and cell viability data, α-DR5 AbCs increased cleaved PARP in RCC4 cells, whereas free α-DR5 antibody, TRAIL, or o42.1 Fc AbCs did not result in an increase in cleaved PARP over baseline (Fig. 4, F and G, shows o42.1 as a representative example; fig. S8, C and E). The α-DR5 AbCs did not significantly induce apoptosis in healthy primary kidney tubular cells (fig. S8, F and G).

Tie-2 pathway activation by Fc-angiopoietin 1 nanocages

Certain receptor tyrosine kinases (RTKs), such as the angiopoietin-1 receptor (Tie2), activate downstream signaling cascades when clustered (*32*, *33*). Scaffolding the F-domain from angiopoietin-1 (A1F) onto nanoparticles induces phosphorylation of AKT and extracellular signal–regulated kinase 1 and 2 (ERK1/2), enhances cell migration and tube formation in vitro, and improves wound healing after injury in vivo (*33*). Therapeutics with these activities could be useful in treating conditions characterized by cell death and inflammation, such as sepsis and acute respiratory distress syndrome. To determine whether the AbC platform could be used to generate such agonists, we assembled o42.1 and i52.3 AbCs with Fc-fusions to A1F (Fig. 4H and fig. S9, A and B). The octahedral and icosahedral A1F-AbCs, but not Fc-only controls or free Fc-Ang1F, significantly increased AKT and ERK1/2 phosphorylation above baseline (Fig. 4, I and J) and enhanced vascular stability (Fig. 4K; fig. S9, C and D; and table S9), comparable to a A1F-presenting octamer generated using a more complex protein conjugation strategy (fig. S9C) (*33*). The o42.1 A1F-Fc AbCs retained activity following incubation for 24 hours in human serum at 4° or 37°C (fig. S9E; precise quantification of the amount retained was complicated by serum background).

α-CD40 nanocages activate B cells

CD40, a TNFR superfamily member expressed on antigen-presenting dendritic cells and B cells, is cross-linked by trimeric CD40 ligand (CD40L or CD154) on T cells, leading to signaling and cell proliferation (*34*, *35*). Nonagonistic α-CD40 antibodies can be converted to agonists by adding cross-linkers such as FcγRIIb-expressing Chinese hamster ovary (CHO) cells (*34*). We investigated whether assembling a nonagonist α-CD40 antibody (LOB7/6) into nanocages could substitute for the need for cell surface presentation; because of its promising data in the DR5 and A1F experiments, we focused on the o42.1 design. Octahedral AbCs were assembled with α-CD40 LOB7/6 IgG (Fig. 5A); SEC and DLS characterization showed these AbCs to be monodisperse and of the expected size (fig. S10, A and B). The octahedral α-CD40 LOB7/6 AbCs induced robust CD40 activation in CD40-expressing reporter CHO cells (J215A, Promega) at concentrations around 1/20 that of a control activating α -CD40 antibody (Promega), whereas no activation was observed for the free LOB7/6 antibody or octahedral AbC formed with non-CD40-binding IgG (Fig. 5B and table S10). Thus, nanocage assembly converts the nonagonist α-CD40 IgG into a CD40 pathway agonist.

α-CD3/28 mosaic nanocages cause T cell proliferation

T cell engineering technologies such as chimeric antigen receptor T cell therapy require the ex vivo expansion and activation of T cells, often carried out by presenting CD3- and CD28-binding ligands on the surface of beads or a plate (*36*, *37*). We sought to eliminate the need for a solid support for T cell activation by using AbCs formed with both α-CD3 and α-CD28 antibodies. Equimolar amounts of α-CD3 and α-CD28 were premixed and then incubated with the o42.1 design to form "mosaic" octahedral cages (Fig. 5A and fig. S10, C and D). Octahedral α-CD3/28 AbC, but not free antibody or Fc nanocage, led to proliferation of naïve T cells sorted from healthy donor peripheral blood mononuclear cells (PBMCs), as read out by expression of the T cell activation marker CD25 (Fig. 5C) and proliferation assays (Fig. 5D); activation levels were similar to tetrameric or plate-bound α-CD3/28 stimulation

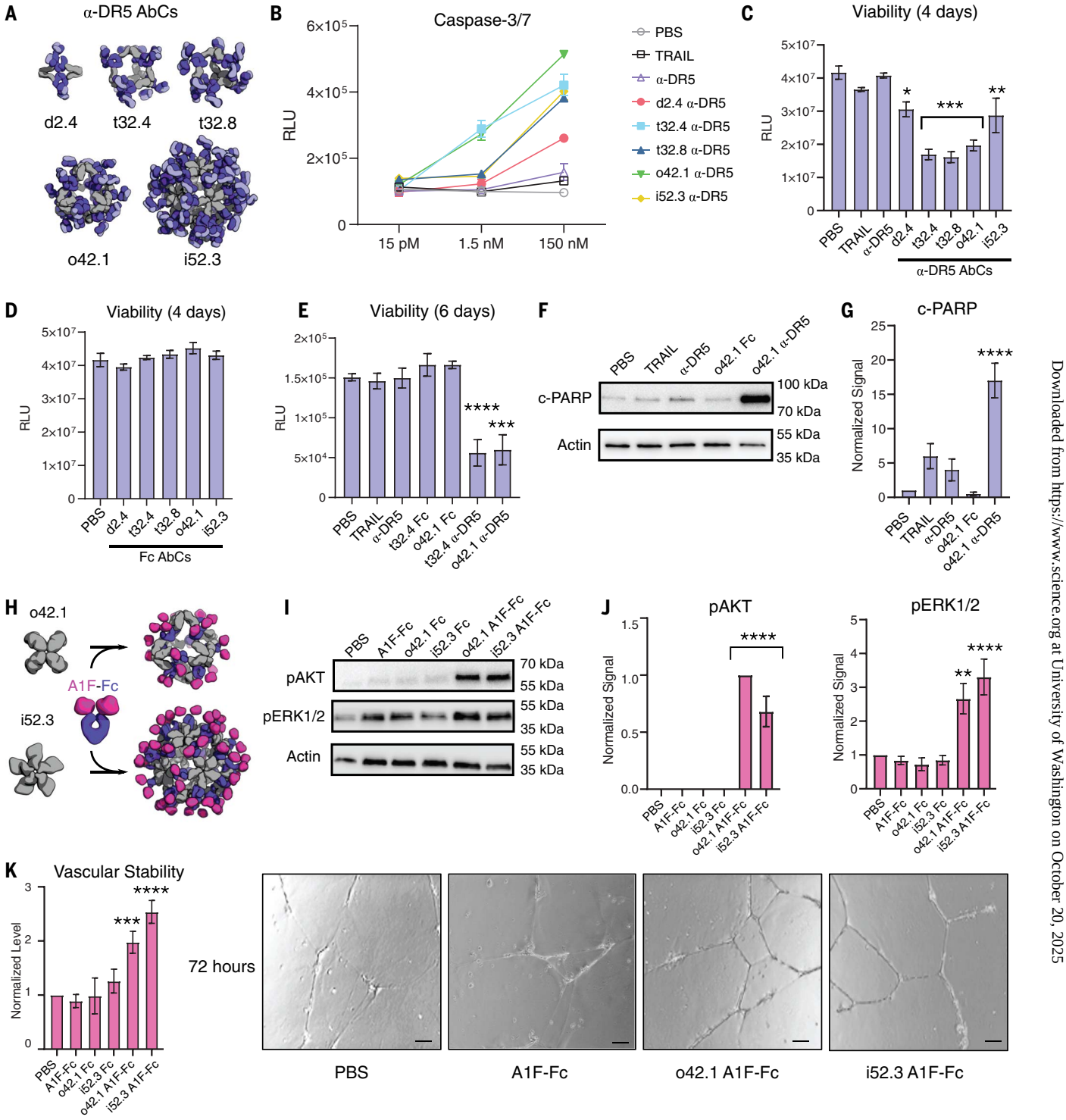

Fig. 4. AbCs activate apoptosis and angiogenesis signaling pathways. (**A** and **B**) Caspase-3/7 is activated by AbCs formed with α-DR5 antibody (A), but not the free antibody, in RCC4 renal cancer cells (B). (**C** and **D**) α-DR5 AbCs (C), but not Fc AbC controls (D), reduce cell viability 4 days after treatment. (**E**) α-DR5 AbCs reduce viability 6 days after treatment. (**F** and **G**) o42.1 α-DR5 AbCs enhance PARP cleavage, a marker of apoptotic signaling; (G) is a quantification of (F) relative to PBS control. (**H**) The F-domain from angiopoietin-1 was fused to Fc (A1F-Fc) and assembled into octahedral (o42.1) and icosahedral (i52.3) AbCs. (**I**) Representative Western blots show that A1F-Fc AbCs, but not controls, increase pAKT and pERK1/2 signals. (**J**) Quantification of (I): pAKT quantification is normalized to o42.1 A1F-Fc signaling (no pAKT signal in the PBS control); pERK1/2 is normalized to PBS. (**K**) A1F-Fc AbCs increase vascular stability after 72 hours. (Left) Quantification of vascular stability compared with PBS. (Right) Representative images; scale bars, 100 μm. All error bars represent means ± SEM; means were compared using analysis of variance and Dunnett post-hoc tests (tables S8 and S9). *$P \leq 0.05$; **$P \leq 0.01$; ***$P \leq 0.001$; ****$P \leq 0.0001$.

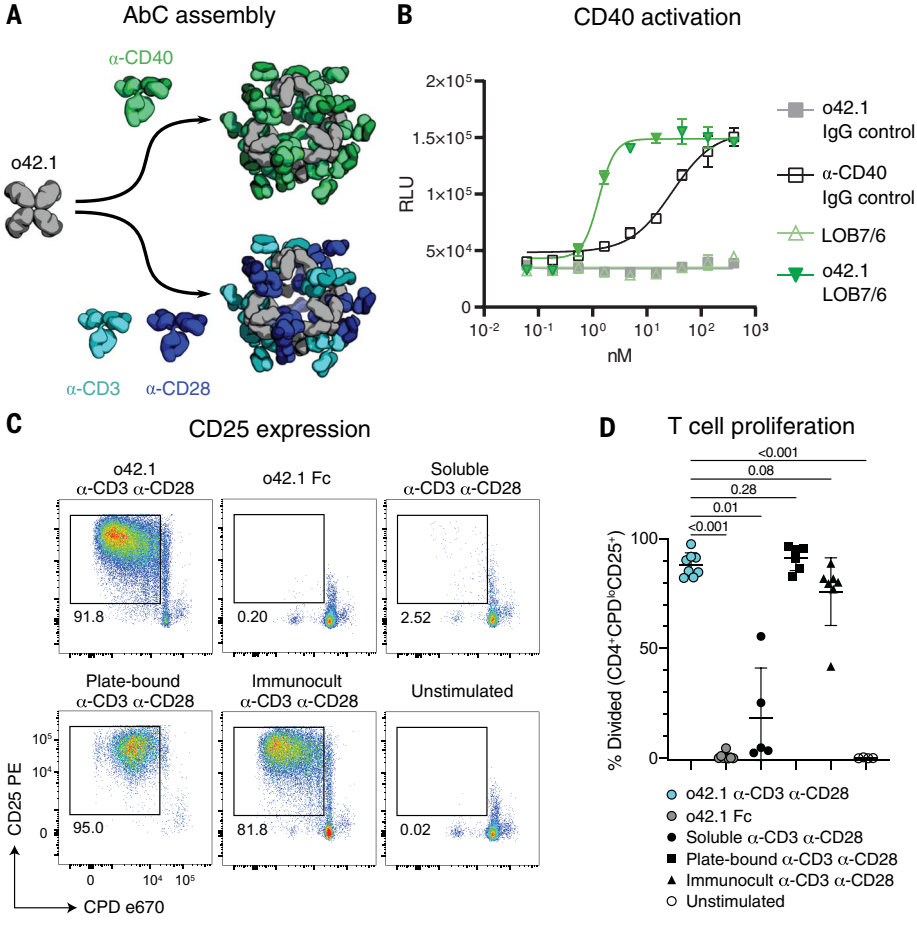

Fig. 5. Activation of immune cells by α-CD40 and α-CD3/28 AbCs. (**A**) Octahedral AbCs are produced with either α-CD40 or premixed α-CD3 and α-CD28 antibodies. (**B**) CD40 pathways are activated by α-CD40 LOB7/6 octahedral nanocages but not by free α-CD40 LOB7/6 or controls. Error bars represent means ± SD, *n* = 3 biological replicates; EC_{50} values are reported in table S10. (**C** and **D**) T cell proliferation and activation are strongly induced by α-CD3 α-CD28 mosaic AbCs compared with unassembled (soluble) α-CD3 α-CD28 antibodies. Representative plots (C) show the frequency of dividing, activated cells ($CPD^{lo}CD25^{+}$). Mosaic AbC-induced proliferation is comparable to traditional positive controls, plate-bound or tetrameric α-CD3 α-CD28 antibody bead complex (Immunocult). Gated on live $CD4^{+}$ T cells. Summary graph (D) shows mean ± SD. Significance was determined by Kruskal-Wallis tests correcting for multiple comparisons using the false discovery rate two-stage method (*n* = 4 to 8 biological replicates per condition). Adjusted *P* values are shown in (D). CPD, Cell Proliferation Dye.

controls. Together with the α-CD40 activation, these results demonstrate how readily specific immune cell pathways can be activated by simply swapping different antibodies into the cage architecture.

Enhancing viral neutralization with AbCs

Considerable effort is currently being directed toward the development of antibodies targeting the severe acute respiratory syndrome coronavirus 2 (SARS-CoV-2) spike (S) protein for prophylaxis and postexposure therapy for the current COVID-19 pandemic (*13*, *38*–*43*). We hypothesized that assembling α-SARS-CoV-2 antibodies into nanocages could potentially increase their neutralization potency by increasing avidity for viral particles, as multivalency was recently found to increase SARS-CoV-2 neutralization using apoferritin to scaffold binding domains (*13*). Octahedral AbCs (o42.1) formed with the SARS-CoV-2 S-binding antibodies CV1 or CV30 (*38*) were more effective at neutralizing pseudovirus entry into angiotensin-converting enzyme 2 (ACE2)–expressing cells than free CV1 or CV30, dropping the apparent median inhibitory concentration (IC_{50}) by more than 200-fold and around 2.5-fold, respectively (comparing molarity at an antibody-to-antibody level) (Fig. 6, A to C; fig. S11, A and B; and table S11). The potency of a third non-neutralizing antibody, CV3, was unchanged by assembly into the nanocage format (fig. S11C). Assembly into octahedral AbCs of Fc-ACE2, which directly engages the receptor binding domain of the spike protein (*43*), enhanced neutralization around sevenfold compared with free Fc-ACE2 fusion for SARS-CoV-2 pseudovirus and 2.5-fold for SARS-CoV-1 pseudovirus (Fig. 6D; fig. S11, D and E; and table S11).

Discussion

Our approach goes beyond previous computational design efforts to create protein nanomaterials by integrating form and function; whereas previous work has fused functional domains onto assemblies constructed from separate structural components (*2*–*12*, *27*), our AbCs use antibodies as both structural and functional components. By fashioning designed antibody-binding, cage-forming oligomers through rigid helical fusion, a wide range of geometries and orientations can be achieved. This design strategy can be generalized to incorporate other homo-oligomers of interest into cage-like architectures. For example, for vaccine applications, nanocages could be assembled with viral glycoproteins using components terminating in glycoprotein binding domains, or from symmetric enzymes with exposed helices available for fusion to maximize the proximity of active sites working on successive reactions. The AbCs offer considerable advantages in modularity compared with previous fusion of functional domain approaches; any of the thousands of known antibodies can be used to form multivalent cages by mixing with the appropriate design to form the desired symmetric assembly, provided sufficient affinity between protein A and Fc. EM and SEC demonstrate monodispersity comparable to IgM and control over binding domain valency and positioning (*44*).

AbCs show considerable promise as signaling pathway agonists. Assembly of antibodies against RTK- and TNFR-family cell surface receptors into AbCs led to activation of diverse downstream signaling pathways involved in cell death, proliferation, and differentiation. Although antibody-mediated clustering has been previously found to activate signaling pathways (*7*, *28*, *34*), our approach has the advantage of much higher structural homogeneity, allowing more precise tuning of phenotypic effects and more controlled formulation. Two or more different receptor-engaging antibodies or Fc-fusions can be readily incorporated into the same cage by simple mixing, allowing exploration of the effects on downstream signaling of bringing together different receptors and comodulators in different valencies and geometries. There are exciting applications to targeted delivery, as the icosahedral AbCs have substantial internal volume (~15,000 nm^3, based on an estimated interior radius of 15.5 nm) that could be used to package nucleic acid or protein cargo, and achieving different target specificity in

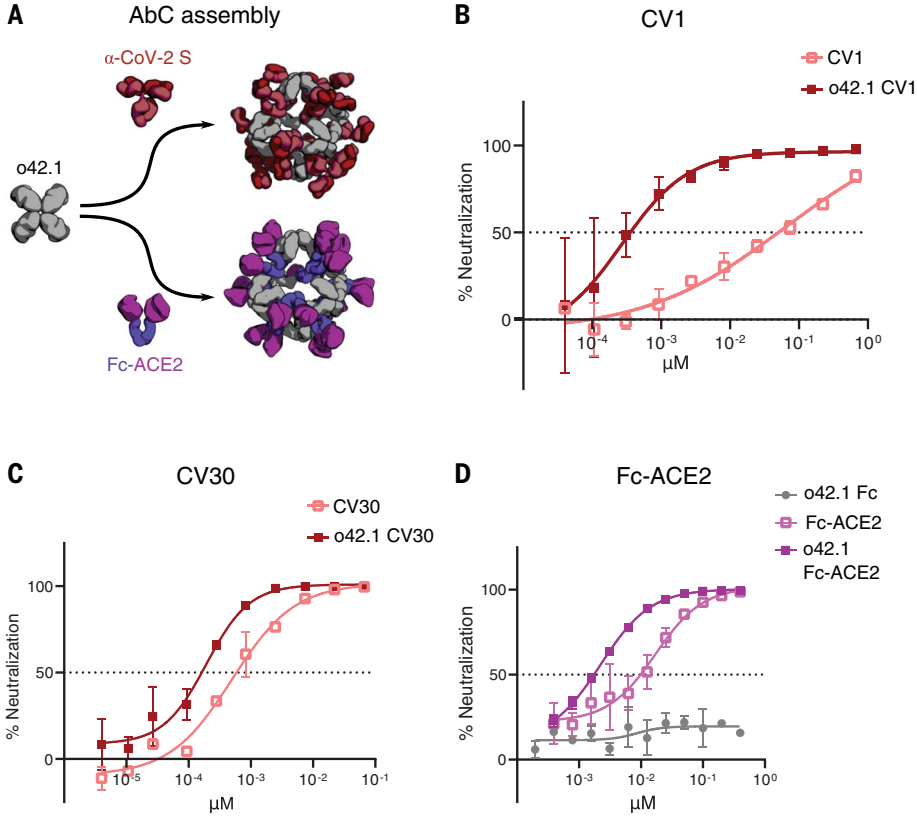

Fig. 6. Nanocage assembly enhances SARS-CoV-2 pseudovirus neutralization. (**A**) Octahedral AbCs are produced with either α-CoV-2 S IgGs or Fc-ACE2 fusion. (**B** and **C**) SARS-CoV-2 S pseudovirus neutralization by octahedral AbC formed with α-CoV-2 S IgGs CV1 (B) or CV30 (C) compared with uncaged IgG. (**D**) SARS-CoV-2 S pseudovirus neutralization by Fc-ACE2 octahedral AbC compared with uncaged Fc-ACE2. Error bars represent means ± SD, n = 2 biological replicates; IC_{50} values are reported in table S11.

principle is as simple as swapping one antibody for another. An important next step toward the possibility of augmenting antibody therapeutics with our designed AbC-forming oligomers will be investigating the pharmacokinetic and biodistribution properties of these molecules, their immunogenicity, and whether the Fc domains can still activate effector functions [while the Fc hinge region is buried in the cage interface, the AbC architecture should not block Fcγ receptors or C1q from binding to N-terminal residues in the Fc CH2 domains (*45*)]. We anticipate that the AbCs developed here, coupled with the very large repertoire of existing antibodies, will be broadly useful across a wide range of applications in biology and medicine.

Materials and methods

Computational design and testing of Fc-binder helical repeat protein (DHR79-FcB)

The crystal structure of the B-domain from *Staphylococcus aureus* protein A in complex with Fc fragment [Protein Data Bank (PDB) ID 1L6X] was relaxed with structure factors using Phenix Rosetta (*46*, *47*). The RosettaScripts MotifGraft mover was used to assess suitable solutions to insertions of the protein A binding motif extracted from 1L6X into a previously reported designed helical repeat protein (DHR79) (*19*). Specifically, a minimal protein A binding motif was manually defined and extracted and used as a template for full backbone alignment of DHR79 while retaining user-specified hotspot residues that interact with the Fc domain in the crystal structure at the Fc/DHR interface and retaining native DHR residues in all other positions. The MotifGraft alignment was followed by five iterations of FastDesign and five iterations of FastRelax in which the DHR side chain and backbone rotamers were allowed to move while the Fc context was completely fixed. The best designs were selected on the basis of a list of heuristic filter values. Figure S1A shows the design model of DHR79-FcB.

Designs were initially assessed via yeast surface display binding to biotinylated Fc protein; yeast display procedures followed previously published protocols (*48*). Upon confirmation of a qualitative binding signal, the design was cloned into a pET29b expression vector with a C-terminal His-tag. The protein was expressed in BL21 DE3 in autoinduction medium (6 g tryptone, 12 g yeast extract, 10 ml 50×M, 10 ml 50×5052, 1 ml 1M $MgSO_4$, 100 μl Studier Trace metals, 50 μg kanamycin antibiotic, brought to a final volume of 500 ml using filtered water) for 20 hours at 27°C at 225 revolutions per minute (rpm); 50×M, 50×5052, and Studier trace metals were prepared according to previously published recipes (*49*). Cells were resuspended in lysis buffer [20 mM Tris, 300 mM NaCl, 30 mM imidazole, 1 mM phenylmethylsulfonyl fluoride (PMSF), 5% glycerol (v/v), pH 8.0] and lysed using a microfluidizer at 18,000 psi. Soluble fractions were separated via centrifugation at 24,000*g*. IMAC with Ni-NTA batch resin was used for initial purification; briefly, nickel-nitrilotriacetic acid (Ni-NTA) resin was equilibrated with binding buffer (20 mM Tris, 300 mM NaCl, 30 mM imidazole, pH 8.0), soluble lysate was poured over the columns, columns were washed with 20 column volumes (CVs) of binding buffer and eluted with 5 CVs of elution buffer (20 mM Tris, 300 mM NaCl, 500 mM imidazole, pH 8.0). SEC with a Superdex 200 column was used as the polishing step (fig. S1B). SEC buffer was 20 mM Tris/HCl pH 7.4, 150 mM NaCl.

Affinity of DHR79-FcB to biotinylated IgG1 and biotinylated Fc protein bound to streptavidin plates was assessed using Octet Biolayer Interferometry (BLI). Data were fit using a 1:1 binding mode. Both 1:1 and 2:1 binding stoichiometries were assessed, and it was determined that the 1:1 binding mode better accounted for the noise in the experiment. This was tested on the Fc binder monomer before any Fc binder-oligomer fusions were made. DHR79-FcB exhibits a 71.7 nM affinity to IgG1 (full antibody) and a 113 nM affinity to the IgG1 Fc protein (fig. S1C).

Computational design of antibody nanocages (AbCs)

Input .pdb files were compiled to use as building blocks for the generation of antibody cages. For the protein A binder model, the domain D from *S. aureus* protein A (PDB ID 1DEE) was aligned to the B-domain of protein A bound to Fc (PDB ID 1L6X) (*18*, *46*). The other Fc-binding design structure, where protein A was grafted onto a helical repeat protein, was also modeled with Fc from 1L6X. PDB file models for monomeric helical repeat protein linkers (42) and cyclic oligomers (two C2s, three C3s, one C4, and two C5s) that had at least been validated via SAXS were compiled from previous work from our lab (*19*–*21*). Building block models were manually inspected to determine which amino acids were suitable for making fusions without disrupting existing protein-protein interfaces.

These building blocks were used as inputs, along with the specified geometry and fusion orientation, into the alpha helical fusion software ["WORMS," ran using instructions provided in Zenodo (*50*); also see supplementary

materials for a description of how to operate WORMS and see Zenodo (*51*) for examples] (*14*, *15*). Fusions were made by overlapping helical segments at all possible allowed amino acid sites. Fusions were then evaluated for deviation for which the cyclic symmetry axes intersect according to the geometric criteria: D2, T32, O32, O42, I32, and I52 intersection angles are 45.0°, 54.7°, 35.3°, 45.0°, 20.9°, and 31.7°, respectively (*22*), with angular and distance tolerances of at most 5.7° and 0.5 Å respectively. Postfusion .pdb files were manually filtered to ensure that the N-termini of the Fc domains are facing outward from the cage, so that the Fabs of an IgG would be external to the cage surface. Sequence design was performed using Rosetta symmetric sequence design (SymPackRotamersMover in RosettaScripts) on residues at and around the fusion junctions (*52*), with a focus on maintaining as many of the native residues as possible. Residues were redesigned if they clashed with other residues or if their chemical environment was changed after fusion (e.g., previously core facing residues were now solvent-exposed). Index residue selectors were used to prevent design at Fc residue positions. See data S4 for an example .xml file used in postfusion design.

Protein expression for AbC-forming designs and Fc constructs

Bacterial expression of AbC-forming designs

Genes were codon optimized for bacterial expression of each designed AbC-forming oligomer, with a C-terminal Gly-Ser linker and 6× C-terminal histidine tag appended. Synthetic genes were cloned into pet29b+ vectors between NdeI and XhoI restriction sites; the plasmid contains a kanamycin-resistant gene and T7 promoter for protein expression. Plasmids were transformed into chemically competent Lemo21(DE3) *E. coli* bacteria using a 15-s heat shock procedure as described by the manufacturer (New England Biolabs). Transformed cells were added to auto-induction expression media, as described above, and incubated for 16 hours at 37°C and 200 rpm shaking (*49*). Cells were pelleted by centrifugation at 4000*g* and resuspended in lysis buffer (150 mM NaCl, 25 mM Tris-HCl, pH 8.0, added protease inhibitor and DNAse). Sonication was used to lyse the cells at 85% amplitude, with 15 s on/off cycles for a total of 2 min of sonication time. Soluble material was separated by centrifugation at 16,000*g*. IMAC was used to separate out the His-tagged protein in the soluble fraction as described above. IMAC elutions were concentrated to ~1 ml using 10K MWCO spin concentrators, filtered through a 0.22 μM spin filter, and run over SEC as a final polishing step (SEC running buffer: 150 mM NaCl, 25 mM Tris-HCl, pH 8.0).

Production of Fc and Fc-fusions

Synthetic genes were optimized for mammalian expression and subcloned into the CMV/R vector (VRC 8400) (*53*). XbaI and AvrII restriction sites were used for insertion of the target gene (Fc, GFP-Fc, RFP-Fc, or A1F-Fc). Gene synthesis and cloning was performed by GenScript. Expi293F cells were grown in suspension using Expi293 Expression Medium (Thermo Fisher Scientific) at 150 rpm, 5% CO_2, 70% humidity, 37°C. At confluency of ~2.5 × 10^6 cells/ml, the cells were transfected with the vector encoding the Fc or Fc-fusion (1000 μg per liter of cells) using PEI MAX (Polysciences) as a transfection reagent. Cells were incubated for 96 hours, after which they were spun down by centrifugation (4000*g*, 10 min, 4°C) and the protein-containing supernatant was further clarified by vacuum-filtration (0.45 μm, Millipore Sigma). In preparation for nickel-affinity chromatography steps, 50 mM Tris, 350 mM NaCl, pH 8.0 was added to the clarified supernatant. For each liter of supernatant, 4 ml of Ni Sepharose excel resin (GE) was added to the supernatant, followed by overnight shaking at 4°C. After 16 to 24 hours, resin was collected and separated from the mixture and washed twice with 50 mM Tris, 500 mM NaCl, 30 mM imidazole, pH 8.0 before elution of desired protein with 50 mM Tris, 500 mM NaCl, 300 mM imidazole, pH 8.0. Eluates were purified by SEC using a Superdex 200 Increase column.

Structural evaluation of AbC-forming designs

Designs that produced monodisperse SEC peaks around their expected retention volume were combined with Fc from hIgG1. Cage components were incubated at 4°C for a minimum of 30 min. During assembly, 100 mM L-arginine was added to AbCs formed with the i52.6 design, as this was observed to maximize the formation of the designed AbC I52 and prevent the formation of visible "crashed out" aggregates (*23*). Fc-binding and cage formation were confirmed via SEC; earlier shifts in retention time (compared with either component run alone) show the formation of a larger structure. NS-EM was used as described below to confirm the structures of designs that passed these steps.

For confirming AbC structures with intact IgGs, hIgG1 was combined with AbC-forming designs following the same protocol for making Fc cages. This assembly procedure was also followed for all IgG or Fc-fusion AbCs reported hereafter. The data in Fig. 2, D and E, show AbCs formed with the α-DR5 antibody AMG-655 (*23*) for the following designs: d2.3, d2.4, d2.7, t32.4, t32.8, o42.1, and i52.3. The data for the i52.6 design shown in Fig. 2, D and E, are from AbCs formed with the hIgG1 antibody mpe8 (*54*); this was simply because of limited AMG-655 availability at the time of the experiment and not a reflection on i52.6/AMG-655 assembly competency. Tables S12 and S13 show the list of IgGs and Fc-fusions that have been formed into AbCs. Table S14 lists the amino acid sequences of all successful AbC-forming designs. Table S15 lists the amino acid sequences of Fc and Fc-fusions used in the following experiments.

SAXS

Samples were prepared for SAXS analysis by first expressing and purifying AbCs with Fc as described above. Fc AbCs were purified via SEC into 150 mM NaCl and 25 mM Tris-HCl at pH 8.0. Fractions corresponding to the Fc AbC peak after SEC were combined, and glycerol was added at 2% final concentration. Samples were concentrated to between 1 and 3 mg/ml using a 10K molecular weight cut-off (MWCO) benchtop spin concentrator. The flow-through was used as a blank for buffer subtraction during SAXS analysis. Proteins were then passed through a 0.22-μm syringe filter (Millipore). These proteins and buffer blanks were shipped to the SIBYLS High Throughput SAXS Advanced Light Source in Berkeley, California, to obtain scattering data (*25*). Scattering traces were fit to theoretical models using the FOXS server (https://modbase.compbio.ucsf.edu/foxs/) (*24*). ScÅtter3 was used for R_g, d_{max}, q_{max}, and pair distance distribution [$P(r)$] analyses (https://bl1231.als.lbl.gov/scatter/). For the $P(r)$ distributions, the Kullback-Leibler divergence (D) of the experimental data from the design model was calculated; Shannon sampling was used to determine the number of points from which to calculate D (*55*).

NS-EM specimen preparation and data collection of Fc and IgG AbCs

For all samples except o42.1 Fc and i52.3 Fc, 3.0 μl of each SEC-purified sample between 0.008 and 0.014 mg/ml in TBS pH 8.0 was applied onto a 400- or 200-mesh Cu grid glow-discharged carbon-coated copper grids for 20 s, followed by 2× application of 3.0 μl 2% nano-W or UF stain.

For 14 samples (d2.3 Fc, d2.4 Fc, d2.7 Fc, t32.4 Fc, t32.8 Fc, i52.6 Fc, d2.3 Fc, d2.4 IgG, d2.7 IgG, t32.4 IgG, t32.8 IgG, o42.1 IgG, i52.3 IgG, and i52.6 IgG samples), micrographs were recorded using Leginon software (*56*) on a 120 kV FEI Tecnai G2 Spirit with a Gatan Ultrascan 4000 4k × 4k CCD camera at 67,000 nominal magnification (pixel size: 1.6 Å per pixel) or 52,000 nominal magnification (pixel size: 2.07 Å) at a defocus range of 1.0 to 2.5 μm (table S3).

For d3.08 Fc and d3.36 Fc samples, micrographs were recorded via manual acquisition on a 120 kV FEI L120C Talos TEM with a 4K × 4K Gatan OneView camera at 57,000 nominal magnification (pixel size: 2.516 Å per pixel) at a defocus range of 1.0 to 2.5 μm.

NS-EM data analysis of Fc and IgG AbCs

Particles were picked either with DoGPicker within the Appion interface (*57*) or cisTEM (*58*); both are reference-free pickers. Contrast-transfer function (CTF) was estimated using GCTF (*59*) or cisTEM. 2D class averages were generated in cryoSPARC (*60*) or in cisTEM. Reference-free ab initio 3D reconstruction using particles selected from 2D class averages from each dataset was performed in cryoSPARC or in cisTEM (table S4).

Cryo-EM specimen preparation and data collection of o42.1 and i52.3 AbCs

Three microliters of o42.1 Fc sample at 0.8 mg/ml in TBS pH 8.0 with 100 mM arginine was applied onto glow-discharged 1.2-μm C-flat copper grids. Three microliters of i52.3 Fc sample at 0.1 mg/ml in TBS pH 8.0 was applied onto glow-discharged 1.2-μm C-flat copper grids coated with a thin layer of continuous home-made carbon. Grids were then plunge-frozen in liquid ethane and cooled with liquid nitrogen using an FEI MK4 Vitrobot with a 6-s blotting time and 0 force for o42.1 Fc, and 2.5-s blotting time and −1 force for i52.3 Fc. The blotting process took place inside the Vitrobot chamber at 20°C and 100% humidity. Data acquisition was performed with the Leginon data collection software on an FEI Glacios electron microscope at 200 kV and a Gatan K2 Summit camera. The nominal magnification was 36,000 with a pixel size of 1.16 Å per pixel. The dose rate was adjusted to 8 counts per pixel per second. Each movie was acquired in counting mode fractionated in 50 frames of 200 ms per frame.

Cryo-EM data analysis of o42.1 and i52.3 AbCs

For both o42.1 Fc and i52.3 Fc datasets, micrographs were motion-corrected using Warp (*61*) and exported to cryoSPARC for CTF estimation with CTFFIND4. A manually picked set of particles was used to generate 2D class averages that were subsequently used (after low-pass filtering to 20-Å resolution) for Template Picker in cryoSPARC on the whole dataset. Particles were extracted with a box size of 648 pixels and subjected to reference-free 2D classification in cryoSPARC.

For the o42.1 Fc dataset, particles from selected 2D classes were classified using ab initio reconstruction in cryoSPARC with default parameters, four classes, and no symmetry imposed. Micrographs containing particles from two classes out of four resulting ab initio classes were subjected to Manually Curate Exposures function in cryoSPARC to remove bad micrographs. This set of particles, after manual curation in cryoSPARC, underwent another round of ab initio reconstruction in cryoSPARC with default parameters, four classes, and no symmetry imposed. One class (4032 particles) from these four resulting ab initio classes was selected for Non-uniform refinement (NUR) in cryoSPARC with no symmetry applied or with O symmetry applied. The NUR map with no symmetry has a 17.7-Å resolution, and the NUR map with O symmetry applied has a 11.14-Å resolution; both maps were similar, justifying imposing O symmetry for the final reconstruction.

For the i52.3 Fc dataset, after one round of 2D classification in cryoSPARC, the micrographs containing particles in a set of selected 2D classes were subjected to Manually Curate Exposures function in cryoSPARC to remove bad micrographs. This set of particles after manual curation in cryoSPARC were subjected to another round of 2D classification in cryoSPARC. A total of 3918 particles from selected 2D classes were reconstructed into one 3D class using ab initio reconstruction in cryoSPARC with no symmetry imposed, maximum and initial resolutions set to 6 and 12 Å respectively, initial and final minibatch sizes set to 1000 images. The resulting C1 ab initio map and particles then underwent NUR in cryoSPARC with no symmetry applied or with I symmetry applied. The NUR map with no symmetry has a 18.44-Å resolution, and the NUR map with I symmetry applied has a 12.18-Å resolution; both maps were similar, justifying imposing I symmetry for the final reconstruction.

All resolutions are reported on the basis of the gold-standard Fourier shell correlation FSC (GSFSC) = 0.143 criterion (*62*, *63*), and FSC curves were corrected for the effects of soft masking by high-resolution noise substitution (*64*). A summary of EM data acquisition and processing is provided in tables S3 and S4.

Computational design of AbCs concurrent with oligomer design

Given the success in designing AbCs when using only previously validated oligomers, we were curious whether we could design structures with newly designed cyclic oligomers. This has the advantage of creating oligomer building blocks for future applications as well as additional AbCs. First, C3s were generated by docking helical proteins into cyclic symmetries and designing a low-energy de novo interface (*20*). Those C3s were used to design 48 AbCs across D3 dihedral (14), T32 tetrahedral (11), O32 octahedral (15), and I32 icosahedral (8) symmetries following the same fusion and design approach described above. From these designs, 36 were soluble, and two D3 dihedra (fig. S5A) formed with Fc into structures very similar to the designed models according to SEC, SAXS, and NS-EM (fig. S5, B to E).

Stability experiments

Samples were prepared for stability analysis by mixing equimolar amounts of each AbC-forming design component with hIgG1 Fc domain. These were purified using SEC using a Superose 6 column, following similar techniques as described above, into TBS (150 mM NaCl, 25 mM Tris-HCl, pH 8.0) with 50 mM L-arginine (from a 1 M L-arginine, pH 8.0); L-arginine was added to all designs as it had been observed to reduce hydrophobic association for the i52.6 AbCs. After SEC, the fractions corresponding to the AbC (leftmost peak) were pooled. These were incubated at room temperature and analyzed once per week for up to 5 weeks post-SEC via DLS and SDS-PAGE. Design d2.3 and d2.4 experiments were started 3 weeks later than the other six designs.

Dynamic light scattering

DLS measurements were performed using the default Sizing and Polydispersity method on the UNcle (Unchained Labs). AbCs (8.8 μl) were pipetted into the provided glass cuvettes. DLS measurements were run in triplicate at 25°C with an incubation time of 1 s; results were averaged across runs and plotted using GraphPad Prism. Table S6 provides DLS summary data.

SDS-PAGE

Fc AbCs (10 μl) were diluted to ~0.1 mg/ml and prepared for SDS by mixing with 2 μl of 6× loading dye (197 mM Tris-HCl, pH 6.8; 70% glycerol; 6.3% SDS; 0.03% bromophenol blue); these were then heated for 5 to 10 min at 95°C and loaded into the wells of a Tris-Glycine gel (Bio-Rad, catalog #5678125). SDS running buffer was prepared to a final concentration of 5 mM Tris, 192 mM glycine, 0.1% SDS, pH 8.3. Two to five microliters of ladder was also added (BioRad 161-0377 or 161-0374). The gel was run for 25 to 30 min at 180 to 200 V or until the dye reached near the bottom of the gel. Gels were stained with Coomassie Brilliant Blue dye using the GenScript eStain protein staining system.

Exchange experiments

GFP-Fc and RFP-Fc were produced in Expi293F cells and purified as described above. GFP-Fc was mixed with o42.1 tetramer; a premixed ratio of RFP-Fc and GFP-Fc (at a 25:1 molar ratio) was separately combined with o42.1 tetramer as a positive control meant to mimic 100% exchange (as the GFP-Fc o42.1 AbC would be mixed with 25-fold excess RFP-Fc). Fc-GFP o42.1 and 25:1 Fc-RFP:GFP o42.1 were purified via a Superose 6 SEC column into TBS (150 mM NaCl, 25 mM Tris-HCl, pH 8.0) with 50 mM L-arginine. Fc-GFP o42.1 was then incubated with 25-fold excess Fc-RFP at a final volume of 2 ml and separated using an autosampler set to inject 470 μl; the autosampler was necessary to control injection volume (Cytiva ALIAS autosampler). Time points were taken at 5 min, 2 hours, 4 hours, and 24 hours after mixing and incubation at 25°C. Controls were GFP-Fc o42.1

without added Fc-RFP, Fc-RFP without AbC, and the "pre-exchanged" control normalized to the GFP-Fc o42.1 molarity. 100 µl from each peak fraction were then added to a 96-well fluorescence plate (Corning, black polystyrene). To measure GFP signal, excitation and emission wavelengths were set to 485 and 510, respectively; for RFP signal, excitation and emission wavelengths were set to 558 and 605, respectively; fluorescence readings were taken with the Neo2 Microplate Reader (BioTek).

DR5 and A1F-Fc experiments

Cell culture

Colorectal adenocarcinoma cell line-Colo205 was obtained from ATCC. Renal cell carcinoma cell line RCC4 (RCC4-pBABE) was a gift from W. Kaelin (Dana-Farber/Harvard Cancer Institute) (*65*). Primary kidney tubular epithelial cells RAM009 were a gift from S. Akilesh (University of Washington). They were derived from a 52-year-old male. The study (#1297) and consent forms were approved by the University of Washington's IRB. Colo205 cells were grown in RPMI1640 medium with 10% fetal bovine serum (FBS) and penicillin/streptomycin. RCC4 cells were grown in Dulbecco's modified eagle's medium (DMEM) with 10% FBS and penicillin/streptomycin. RAM009 were grown in RPMI with 10% FBS, ITS-supplement, penicillin/streptomycin, and nonessential amino acids. All cell lines were maintained at 37°C in a humidified atmosphere containing 5% CO_2.

Human umbilical vein endothelial cells (HUVECs, Lonza, Germany, #C2519AS) were grown on 0.1% gelatin-coated 35-mm cell culture dish in EGM2 media. Briefly, EGM2 consist of 20% FBS, 1% penicillin-streptomycin, 1% Glutamax (Gibco, #35050061), 1% endothelial cell growth factor (*32*), 1 mM sodium pyruvate, 7.5 mM HEPES, 0.08 mg/mL heparin, 0.01% amphotericin B, a mixture of 1× RPMI 1640 with and without glucose to reach 5.6 mM glucose concentration in the final volume. Media was filtered through a 0.45-µm filter. HUVECs at passage 7 were used in Tie2 signaling experiments. HUVECs at passage 6 were used in the tube formation assay.

Caspase-Glo 3/7 and Caspase-Glo 8 assays

Cells were passaged using trypsin and 40,000 cells per well were plated onto a 96-well white tissue culture plate and grown in appropriate media. Medium was changed the next day (100 µl per well) and cells were treated with either uncaged α-DR5 AMG655 antibody (150 nM), recombinant human TRAIL (150 nM), Fc-only AbCs or α-DR5 AbCs (150 nM, 1.5 nM, 15 pM for caspase-3/7; only 150 nM and 1.5 nM were tested for caspase-8) and incubated at 37°C for 24 hours (caspase-3/7) or 12 hours (caspase-8). In all cases here and throughout, the antibody or AbC concentration refers to the protein's asymmetric unit (e.g., the molar unit for the antibody is one heavy chain and one light chain). The next day, 100 µl per well of Caspase-Glo 3/7 reagent or Caspase-Glo 8 reagent (Promega, USA) were added into the media and incubated for 1 hour (caspase-3/7) or 2 hours (caspase-8) at 37°C. Luminescence was then recorded using Perkin EnVision microplate reader (Perkin Elmer). Statistical comparisons were performed using GraphPad Prism (see table S8 for full details).

CellTiter-Glo cell viability assay (4-day viability)

Cells were plated onto a 96-well plate at 20,000 cells per well. The next day, cells were treated with 150 nM of α-DR5 AbCs, TRAIL, and α-DR5 antibody for 4 days. At day 4, 100 µl of CellTiter-Glo reagent (Promega Corp. USA, #G7570) was added to the 100 µl of media per well, incubated for 10 min at 37°C, and luminescence was measured using a Perkin-Elmer Envision plate reader.

AlamarBlue cell viability assay (6-day viability)

Cells were seeded onto a 12-well tissue culture plate at 50,000 cells/well. The next day, cells were treated with α-DR5 AbCs, TRAIL, or α-DR5 antibodies at 150 nM concentration. Three days later, cells were passaged at 30,000 cells per well and treated with 150 nM of α-DR5 cages, TRAIL, and α-DR5 antibody for 3 days. At 6 days, the media was replaced with 450 µl per well of fresh media and 50 µl of alamarBlue reagent (Thermo Fisher Scientific, USA, #DAL1025) was then added. After 4 hours of incubation at 37°C, 50 µl of media were transferred into a 96-well opaque white plate and fluorescence intensity was measured using plate reader according to manufacturer's instructions.

Protein isolation for Western blot analysis

Cells were passaged onto a 12-well plate at 80,000 cells per well and were grown until 80% confluency was reached. Before treatment, the media was replaced with 500 µl of fresh media. For DR5 experiments, AMG-655 antibody and TRAIL were added at 150 nM concentration, and Fc-only nanocages or α-DR5 nanocages were added at 150 nM, 1.5 nM, and 15 pM concentration onto the media and incubated for 24 hours at 37°C prior protein isolation; as above, concentrations are calculated on the basis of the asymmetric unit. For the caspase inhibition experiment, RCC4 cells were pretreated for 30 min with 10 µM of zVAD followed by treatment with 150 nM o42.1 α-DR5 Ab for additional 24 hours and total protein isolation.

Media containing dead cells was transferred to a 1.5 ml Eppendorf tube, and the cells were gently rinsed with 1× phosphate-buffered saline (PBS). Trypsin (1×) was added to the cells for 3 min. All the cells were collected into the 1.5-ml Eppendorf containing the medium with dead cells. Cells were washed once in PBS 1× and lysed with 70 µl of lysis buffer containing 20 mM Tris-HCl (pH 7.5), 150 mM NaCl, 15% glycerol, 1% Triton, 3% SDS, 25 mM β-glycerophosphate, 50 mM NaF, 10 mM sodium pyrophosphate, 0.5% orthovanadate, 1% PMSF (all chemicals were from Sigma-Aldrich, St. Louis, MO), 25 U Benzonase Nuclease (EMD Chemicals, Gibbstown, NJ), protease inhibitor cocktail (PierceTM Protease Inhibitor Mini Tablets, Thermo Scientific, USA), and phosphatase inhibitor cocktail 2 (#P5726), in their respective tubes). Total protein samples were then treated with 1 µl of Benzonase (Novagen, USA) and incubated at 37°C for 10 min. Laemmli Sample buffer (21.6 µl of 4×; Bio-Rad, USA) containing 10% beta-mercaptoethanol was added to the cell lysate and then heated at 95°C for 10 min. The boiled samples were either used for Western blot analysis or stored at −80°C.

Western blotting

The protein samples were thawed and heated at 95°C for 10 min. Ten microliters of protein sample per well was loaded and separated on a 4 to 10% SDS-PAGE gel for 30 min at 250 V. The proteins were then transferred onto a nitrocellulose membrane for 12 min using the semi-dry turbo transfer Western blot apparatus (Bio-Rad, USA). Post-transfer, the membrane was blocked in 5% nonfat dry milk for 1 hour. After 1 hour, the membrane was probed with the respective antibodies: cleaved-PARP (Cell Signaling, #9541, USA) at 1:2000 dilution; Cleaved-caspase 8 (Cell Signaling, #9496, USA) at 1:2000 dilution; pERK1/2 (Cell Signaling) at 1:5000 dilution; pFAK (Cell Signaling) at 1:1000 dilution; p-AKT(S473) (Cell Signaling) at 1:2000 dilution; and actin (Cell Signaling, USA) at 1:10,000 dilution. Separately, for p-AKT (S473) the membrane was blocked in 5% BSA for 3 hours followed by primary antibody addition. Membranes with primary antibodies were incubated on a rocker at 4°C, overnight. Next day, the membranes were washed with 1× TBST (three times, 10-min interval), and the respective HRP-conjugated secondary antibody (Bio-Rad, USA) (1:10,000) was added and incubated at RT for 1 hour. For p-AKT(S473), after washes, the membrane was blocked in 5% milk at room temperature for 1 hour and then incubated in the respective HRP-conjugated secondary antibody (1:2000) prepared in 5% milk for 2 hours. After secondary antibody incubation, all the membranes were washed with 1× TBST (three times, 10-min interval). Western blots were developed using Luminol reagent (Immobilon Western Chemiluminescent HRP Substrate, Millipore) for 3 to 15 s and imaged using Bio-Rad ChemiDoc Imager. Data were quantified using the ImageJ software to analyze band intensity.

Quantifications were done by calculating the peak area for each band. Each signal was normalized to the actin quantification from that lane of the same gel, to allow for cross-gel comparisons. Fold-changes were then calculated compared with PBS for all samples except for the pAKT reported for the A1F-Fc Western blot (there was not enough pAKT signal for comparison, so o42.1 A1F-Fc was used for normalization). Statistical comparisons were performed using GraphPad Prism (see tables S8 and S9 for full detail). For all statistical analyses, means were compared with the PBS condition.

Tube formation assay (vascular stability)

Vascular stability and tube formation were assessed using a protocol modified from a previous report (*66*). Briefly, passage 6 HUVECs were seeded onto 24-well plates precoated with 150 μl of 100% cold Matrigel (Corning, USA) at a density of 150,000 cells per well, along with scaffolds at 89 nM F-domain concentrations or PBS in low-glucose DMEM medium supplemented with 0.5% FBS for 24 hours. At the 24-hour time point, old media was aspirated and replaced with fresh media without added AbCs or controls. The cells were incubated up to 72 hours. Cells were imaged at 48- and 72-hour time points using Leica Microscope at 10× magnification under phase contrast. Thereafter, the tubular formations were quantified by calculating the number of nodes, meshes and tubes using the Angiogenesis Analyzer plugin in Image J software. Vascular stability was calculated by averaging the number of nodes, meshes, and tubes, and then normalizing to PBS. Statistical comparisons were performed using GraphPad Prism (see table S9 for full detail).

Human serum A1F-Fc AbC incubation experiment

HUVECs (C2519AS, Lonza) were grown to at least 80% confluence in 24-well plate format pretreated with attachment factor (S006100, Thermo Fisher) and cultured in EGM-2 growth medium (CC-3162, Lonza) according to manufacturer's instructions. The cells were then starved in DMEM low-glucose serum-free media (11885084, Gibco) for 24 hours. In parallel, proteins were incubated in 100% human serum (Sigma, H4522-100ML) at 1.5 μM for 24 hours at 4° or 37°C; dilutions of AbC into serum were ~1:4 (AbC to final, v/v). After starvation and protein incubation, cell media was replaced, and proteins were added to the cells at a final concentration of 150 nM for 30 min at 37°C. Conditions with human serum were all normalized to a final concentration of 10% upon addition to the cell media. After treatment, the media was aspirated, and cells were washed once with PBS before lysis. Cells were lysed with 60 μl of lysis buffer containing 50 mM HEPES, 150 mM NaCl, 10% glycerol, 1% Triton X-100, 3% SDS, 25 mM β-glycerophosphate, 100 mM NaF, 10 mM sodium pyrophosphate, 1 mM EGTA, 1.5 mM $MgCl_2$, 1% sodium orthovanadate, 300 μM PMSF, 25 U DNase, 1% phosphatase inhibitor cocktail 2 (all chemicals were from Sigma-Aldrich), and protease inhibitor cocktail (PierceTM Protease Inhibitor Mini Tablets, Thermo Scientific, USA). Cell lysate was collected in a fresh Eppendorf tube. Lysate samples were prepared using the Anti-Rabbit Detection Module for the Jess instrument (ProteinSimple) and boiled for 10 min at 98°C. A 12-to 230-kDa 25-capillary cartridge and microplate were used for the Jess instrument, using the anti-phospho-Akt (S473) (D9E) XP rabbit monoclonal antibody (4060, Cell Signaling) with a 30-min incubation time. Replicate chemiluminescent peak values corresponding to phospho-Akt (~56 kDa) are reported.

Immune cell activation materials and methods

CD40 luminescence assay

A nonagonistic antibody (clone LOB7/6, product code MCA1590T, BioRad), was combined with the octahedral o42.1 AbC-forming design as described above and further characterized by DLS and NS-EM (fig. S10). Negative control o42.1 AbC was made using a non-CD40-binding IgG (mpe8), which binds to respiratory syncytial virus spike protein (*54*). These two AbCs, along with uncaged LOB7/6 and a positive control CD40-activating IgG (Promega, #K118A) were diluted to make a 10-point, threefold dilution series for triplicate technical repeats starting at 1.2 μM; as described above, concentrations are calculated on the basis of the asymmetric unit. The positive control CD40-activating IgG (K118A) is a murine IgG1a antibody, it was not compatible for assembly with the o42.1 design, likely because of the low binding interface between protein A and mIgG1a (data not shown). Particles were filtered using a 0.22-μm syringe filter (Millipore) and AbC formation was assessed using SEC and DLS using procedures described above. SEC was used as an analytical technique to show absence of unassembled components; owing to the expense of commercial antibodies and the typical loss of yield using SEC, as would be expected for any filtration technique, we did not use SEC as a separation technique here before DLS measurements or in vitro assays. SEC and DLS confirm the presence of the designed assemblies and absence of off-target or unassembled species; the o42.1 AbCs eluted in the SEC void of the Superose 6 column as expected given their designed and verified radii (~40 nm when formed with IgGs). Postfiltration concentration readings were taken and confirmed that there was no sample loss when using the syringe filter.

To assay CD40 activation, we followed manufacturer's instructions for a bioluminescent cell-based assay that measures the potency of CD40 response to external stimuli such as IgGs (Promega, JA2151). Briefly, CD40 effector CHO cells were cultured and reagents were prepared according to the assay protocol. The antibodies and AbCs were incubated with the CD40 effector CHO cells for 8 hours at 37°C, 5% CO_2. Bio-Glo Luciferase Assay System (G7941) included in the assay kit is used to visualize the activation of CD40 from luminescence readout from a plate reader. The Bio-Glo reagent is applied to the cells, and luminescence was detected by a Synergy Neo2 plate reader every min for 30 min. Data were analyzed by averaging luminescence between replicates and subtracting plate background. The fold induction of CD40-binding response was determined by the relative luminescent unit (RLU) of sample normalized to RLU of no antibody controls. Data curves were plotted and the median effective concentration (EC_{50}) was calculated using GraphPad Prism using the log(agonist) versus response–Variable slope (four parameters); see table S10 for EC_{50} values and 95% confidence interval (CI) values.

T cell proliferation and flow cytometry

Mosaic AbCs were formed by mixing α-CD3 (clone name: OKT3, BioLegend) and α-CD28 (CD28.6, #16-0288-85, Thermo Fisher) antibodies together first, and then combining with excess o42.1 AbC-forming design. Mosaic α-CD3/28 o42.1 cages were purified via SEC into PBS as described above. SEC and DLS confirmed the assembly of o42.1 AbCs, which eluted as expected into the void volume in SEC given the particle's size.

Primary human PBMCs were obtained upon written informed consent from the Virginia Mason Medical Center in Seattle, Washington, USA. All studies were approved by the Institutional Review Board of the Benaroya Research Institute (Seattle, WA). Naïve $CD4^+$ conventional human T cells ($CCR7^+CD45RA^+CD127^{hi}CD25^{neg}$) were isolated from PBMC by cell sorting to >99% purity. PBMCs were first labeled with 2.5 μM Cell Proliferation Dye (CPD) e670 (Thermo Fisher) according to manufacturer instructions, then rested for 1 hour at 37°C and 5% CO_2. CPD-labeled cells were harvested, incubated with viability dye ef780 (Thermo Fisher), and stained in buffer containing HBBS + 0.3% BSA with indicated fluorescently labeled surface markers. Cell sorting and analysis were performed on a FACSAria Fusion (BD Biosciences) using an 85-μM nozzle at 45 psi. Sorted T cells (1×10^6 ml) were incubated in the presence of indicated stimulation conditions (0.01 μM) in ImmunoCult-XF T Cell Expansion Medium (Stem Cell). After 4 to 5 days, cells were harvested and restained with fluorescent antibodies. Data were analyzed using FlowJo software (Tree Star, Inc.)

Viral neutralization

CV1, CV3, and CV30

α-CoV-2 S cages using CV IgGs were prepared by mixing α-CoV-2 S IgGs with a 1:1 molar ratio of o42.1 design component and purifying via SEC into TBS, following similar protocols to those as described above for AbC assembly.

HIV-1–derived viral particles were pseudotyped with full length wild-type SARS-CoV-2 S (*67*). Briefly, plasmids expressing the HIV-1 Gag and pol (pHDM-Hgpm2, BEI Resources, #NR-52517), HIV-1Rev (pRC-CMV-rev1b, BEI Resources, #NR-52519), HIV-1 Tat (pHDM-tat1b, BEI Resources, #NR-52518), the SARS-CoV-2 spike (pHDM-SARS-CoV-2 Spike, BEI Resources, #NR-52514) and a luciferase/GFP reporter (pHAGE-CMV-Luc2-IRES-ZsGreen-W, BEI Resources, #NR-52516) were cotransfected into 293T cells at a 1:1:1:1.6:4.6 ratio using 293 Free transfection reagent (EMD Millipore, #72181) according to the manufacturer's instructions. Transfected cells were incubated at 32°C for 72 hours, after which the culture supernatant was harvested, clarified by centrifugation, and frozen at −80°C.

HEK293 cells stably expressing ACE2 (HEK-293T-hACE2, BEI Resources, #NR-5251) were seeded at a density of 4×10^3 cells per well in a 100 μl volume in 96-well flat- and clear-bottomed black-walled plates (Greiner Bio-One, #655090) (*67*). The next day, IgG alone, or in complex with cage components, was serially diluted in 30 μl of complete DMEM (cDMEM) in 96-well round-bottomed plates in triplicate; as described above, concentrations were calculated on the basis of the asymmetric unit.

An equal volume of viral supernatant was added to each well and incubated for 60 min at 37°C. Meanwhile, 50 μl of cDMEM containing 6 μg/ml polybrene was added to each well of 293T-ACE2 cells (2 μg/ml final concentration) and incubated for 30 min. The media was aspirated from 293T-ACE2 cells, and 100 μl of the virus-antibody mixture was added. The plates were incubated at 37°C for 72 hours. The supernatant was aspirated and replaced with 100 μl of Steady-Glo luciferase reagent (Promega), and the plate was read on a Fluorskan Ascent Fluorimeter. Control wells containing virus but no antibody (cells + virus) and no virus or antibody (cells only) were included on each plate.

Percent neutralization for each well was calculated as the RLU of the average of the cells + virus wells, minus test wells (cells + IgG + virus), and dividing this result difference by the average RLU between virus control (cells + virus) and average RLU between wells containing cells alone, multiplied by 100. The IC_{50} was interpolated from the neutralization curves determined using the log(inhibitor) versus response–Variable slope (four parameters) fit using GraphPad Prism Software. Experiments were performed in duplicate. See table S4 for IC_{50} values and 95% CI values.

Fc-ACE2

Murine leukemia virus (MLV)–based SARS-CoV-2 S-pseudotyped viruses were prepared as previously described (*43*). Briefly, human embryonic kidney 293T (HEK293T) cells were cotransfected with a SARS-CoV-2 S encoding–plasmid, an MLV Gag-Pol packaging plasmid, and the MLV transfer vector encoding a luciferase reporter using the Lipofectamine 2000 transfection reagent (Life Technologies) according to the manufacturer's protocols. Transfection mixtures were added dropwise to HEK293T cells. Cells were then incubated in the transfection mixture and OPTI-MEM for 5 hours at 37°C with 8% CO_2 before the medium was exchanged into DMEM containing 10% FBS. After 72 hours, the pseudovirus-containing supernatant was collected, centrifuged for 10 min at 3000*g* to clear cell debris, and filtered using a 0.45-μm filter with PES-membrane (MilliporeSigma). The pseudoviruses were concentrated using 30 kDa cut-off concentrators (Amicon) and stored at −80°C until further use.

HEK-293T-hACE2 (BEI Resources, #NR-5251) were cultured in DMEM containing 10% FBS and 1% PenStrep (*67*). Sixteen to twenty-four hours before infection, cells were plated into white-sided clear-bottomed 96-well plates coated with Poly-L-Lysine solution (Sigma Aldrich, #P4707). Briefly, 25 μl Poly-L-Lysine solution was added to each well. The plate was incubated at room temperature for 10 min before removal of Poly-L-Lysine and washing with tissue culture grade water. The Poly-L-lysine–coated plate was dried for 10 min before the cell plating step. Before transfection the HEK-293T-hACE2, 96-well plates were washed three times with DMEM. Fc-ACE2 (Sino Biological, #10108-H02H), o42.1 Fc, and o42.1 Fc-ACE2 were purified via SE,C as described above, and serially diluted 2× in DMEM starting from 800 nM; all concentrations are calculated on the basis of the asymmetric unit. Equal volumes of concentrated pseudovirus and serial dilution of treatments (Fc-ACE2, o42.1 Fc particles or o42.1 Fc-ACE2 particles or DMEM) were combined and incubated for 30 min and then added to the cells. After 2 to 3 hours, DMEM containing 20% FBS and 2% PenStrep was added to the cells. Forty-eight hours after infection, One-Glo-EX (Promega) was added to the cells, and cells were incubated in the dark for 5 to 10 min before reading on a Varioskan LUX plate reader (Thermo Fisher). As above, IC_{50} was interpolated from the neutralization curves determined using the log(inhibitor) versus response–Variable slope (four parameters) using GraphPad Prism Software. The difference in IC_{50} was compared using the extra sum-of-squares *F*-test function in Prism with a *P*-value cutoff at 0.05. Experiments were performed in technical duplicate. See table S11 for IC_{50} values and 95% CI values.

REFERENCES AND NOTES

1. R.-M. Lu *et al*., Development of therapeutic antibodies for the treatment of diseases. *J. Biomed. Sci.* **27**, 1–30 (2020). doi: 10.1186/s12929-019-0592-z; pmid: 31894001
2. A. M. Cuesta, N. Sainz-Pastor, J. Bonet, B. Oliva, L. Alvarez-Vallina, Multivalent antibodies: When design surpasses evolution. *Trends Biotechnol.* **28**, 355–362 (2010). doi: 10.1016/j.tibtech.2010.03.007; pmid: 20447706
3. N. Nuñez-Prado *et al*., The coming of age of engineered multivalent antibodies. *Drug Discov. Today* **20**, 588–594 (2015). doi: 10.1016/j.drudis.2015.02.013; pmid: 25757598
4. N. S. Laursen *et al*., Universal protection against influenza infection by a multidomain antibody to influenza hemagglutinin. *Science* **362**, 598–602 (2018). doi: 10.1126/science.aaq0620; pmid: 30385580
5. O. Seifert *et al*., Tetravalent antibody-scTRAIL fusion proteins with improved properties. *Mol. Cancer Ther.* **13**, 101–111 (2014). doi: 10.1158/1535-7163.MCT-13-0396; pmid: 24092811
6. T. F. Rowley *et al*., Engineered hexavalent Fc proteins with enhanced Fc-gamma receptor avidity provide insights into immune-complex interactions. *Commun. Biol.* **1**, 146 (2018). doi: 10.1038/s42003-018-0149-9; pmid: 30272022
7. R. S. Riley, E. S. Day, Frizzled7 antibody-functionalized nanoshells enable multivalent binding for Wnt signaling inhibition in triple negative breast cancer cells. *Small* **13**, 1700544 (2017). doi: 10.1002/smll.201700544; pmid: 28544579
8. H. J. Kang *et al*., Developing an antibody-binding protein cage as a molecular recognition drug modular nanoplatform. *Biomaterials* **33**, 5423–5430 (2012). doi: 10.1016/j.biomaterials.2012.03.055; pmid: 22542610
9. H. Kim, Y. J. Kang, J. Min, H. Choi, S. Kang, Development of an antibody-binding modular nanoplatform for antibody-guided targeted cell imaging and delivery. *RSC Adv.* **6**, 19208–19213 (2016). doi: 10.1039/C6RA00233A
10. S. I. Lim, C. I. Lukianov, J. A. Champion, Self-assembled protein nanocarrier for intracellular delivery of antibody. *J. Control. Release* **249**, 1–10 (2017). doi: 10.1016/j.jconrel.2017.01.007; pmid: 28069555
11. K. Uhde-Holzem *et al*., Production of immunoabsorbent nanoparticles by displaying single-domain protein a on potato virus X. *Macromol. Biosci.* **16**, 231–241 (2016). doi: 10.1002/mabi.201500280; pmid: 26440117
12. A. Miller, S. Carr, T. Rabbitts, H. Ali, Multimeric antibodies with increased valency surpassing functional affinity and potency thresholds using novel formats. *MAbs* **12**, 1752529 (2020). doi: 10.1080/19420862.2020.1752529; pmid: 32316838
13. E. Rujas *et al*., Multivalency transformsSARS-CoV-2 antibodies into broad and ultrapotent neutralizers. bioRxiv 2020.10.15.341636 [Preprint]. 16 October 2020. https://doi.org/10.1101/2020.10.15.341636.
14. I. Vulovic *et al*., Generation of ordered protein assemblies using rigid three-body fusion. bioRxiv 2020.07.18.210294 [Preprint]. 19 July 2020. https://doi.org/10.1101/2020.07.18.210294.
15. Y. Hsia *et al*., Hierarchical design of multi-scale protein complexes by combinatorial assembly of oligomeric helical bundle and repeat protein building blocks. bioRxiv 2020.07.27.221333 [Preprint]. 28 July 2020. https://doi.org/10.1101/2020.07.27.221333.
16. J. B. Bale *et al*., Accurate design of megadalton-scale two-component icosahedral protein complexes. *Science* **353**, 389–394 (2016). doi: 10.1126/science.aaf8818; pmid: 27463675
17. G. Ueda *et al*., Tailored design of protein nanoparticle scaffolds for multivalent presentation of viral glycoprotein antigens. *eLife* **9**, e57659 (2020). doi: 10.7554/eLife.57659; pmid: 32748788
18. M. Graille *et al*., Crystal structure of a *Staphylococcus aureus* protein A domain complexed with the Fab fragment of a human IgM antibody: Structural basis for recognition of B-cell receptors and superantigen activity. *Proc. Natl. Acad. Sci. U.S.A.* **97**, 5399–5404 (2000). doi: 10.1073/pnas.97.10.5399; pmid: 10805799
19. T. J. Brunette *et al*., Exploring the repeat protein universe through computational protein design. *Nature* **528**, 580–584 (2015). doi: 10.1038/nature16162; pmid: 26675729
20. J. A. Fallas *et al*., Computational design of self-assembling cyclic protein homo-oligomers. *Nat. Chem.* **9**, 353–360 (2017). doi: 10.1038/nchem.2673; pmid: 28338692
21. Y. Hsia *et al*., Design of a hyperstable 60-subunit protein dodecahedron. *Nature* **535**, 136–139 (2016). doi: 10.1038/nature18010; pmid: 27309817

22. T. O. Yeates, Y. Liu, J. Laniado, The design of symmetric protein nanomaterials comes of age in theory and practice. *Curr. Opin. Struct. Biol.* **39**, 134–143 (2016). doi: 10.1016/j.sbi.2016.07.003; pmid: 27476148
23. B. M. Baynes, D. I. C. Wang, B. L. Trout, Role of arginine in the stabilization of proteins against aggregation. *Biochemistry* **44**, 4919–4925 (2005). doi: 10.1021/bi047528r; pmid: 15779919
24. D. Schneidman-Duhovny, M. Hammel, J. A. Tainer, A. Sali, Accurate SAXS profile computation and its assessment by contrast variation experiments. *Biophys. J.* **105**, 962–974 (2013). doi: 10.1016/j.bpj.2013.07.020; pmid: 23972848
25. K. N. Dyer *et al*., High-throughput SAXS for the characterization of biomolecules in solution: A practical approach. *Methods Mol. Biol.* **1091**, 245–258 (2014). doi: 10.1007/978-1-62703-691-7_18; pmid: 24203338
26. K. Mohan *et al*., Topological control of cytokine receptor signaling induces differential effects in hematopoiesis. *Science* **364**, eaav7532 (2019). doi: 10.1126/science.aav7532; pmid: 31123111
27. M. Siegemund *et al*., IgG-single-chain TRAIL fusion proteins for tumour therapy. *Sci. Rep.* **8**, 7808 (2018). doi: 10.1038/s41598-018-24450-8; pmid: 29773864
28. J. D. Graves *et al*., Apo2L/TRAIL and the death receptor 5 agonist antibody AMG 655 cooperate to promote receptor clustering and antitumor activity. *Cancer Cell* **26**, 177–189 (2014). doi: 10.1016/j.ccr.2014.04.028; pmid: 25043603
29. J. Naval, D. de Miguel, A. Gallego-Lleyda, A. Anel, L. Martinez-Lostao, Importance of TRAIL molecular anatomy in receptor oligomerization and signaling. Implications for cancer therapy. *Cancers* **11**, 444 (2019). doi: 10.3390/cancers11040444; pmid: 30934872
30. D. de Miguel, J. Lemke, A. Anel, H. Walczak, L. Martinez-Lostao, Onto better TRAILs for cancer treatment. *Cell Death Differ.* **23**, 733–747 (2016). doi: 10.1038/cdd.2015.174; pmid: 26943322
31. M. H. Tuthill *et al*., TRAIL-R2-specific antibodies and recombinant TRAIL can synergise to kill cancer cells. *Oncogene* **34**, 2138–2144 (2015). doi: 10.1038/onc.2014.156; pmid: 24909167
32. V.-M. Leppänen, P. Saharinen, K. Alitalo, Structural basis of Tie2 activation and Tie2/Tie1 heterodimerization. *Proc. Natl. Acad. Sci. U.S.A.* **114**, 4376–4381 (2017). doi: 10.1073/pnas.1616166114; pmid: 28396439
33. Y. T. Zhao *et al*., F-domain valency determines outcome of signaling through the angiopoietin pathway. bioRxiv 2020.09.19.304188 [Preprint]. 24 December 2020. https://doi.org/10.1101/2020.09.19.304188.
34. R. S. Kornbluth, M. Stempniak, G. W. Stone, Design of CD40 agonists and their use in growing B cells for cancer immunotherapy. *Int. Rev. Immunol.* **31**, 279–288 (2012). doi: 10.3109/08830185.2012.703272; pmid: 22804572
35. R. H. Vonderheide, M. J. Glennie, Agonistic CD40 antibodies and cancer therapy. *Clin. Cancer Res.* **19**, 1035–1043 (2013). doi: 10.1158/1078-0432.CCR-12-2064; pmid: 23460534
36. E. R. Steenblock, S. H. Wrzesinski, R. A. Flavell, T. M. Fahmy, Antigen presentation on artificial acellular substrates: Modular systems for flexible, adaptable immunotherapy. *Expert Opin. Biol. Ther.* **9**, 451–464 (2009). doi: 10.1517/14712590902849216; pmid: 19344282
37. J. V. Kim, J.-B. Latouche, I. Rivière, M. Sadelain, The ABCs of artificial antigen presentation. *Nat. Biotechnol.* **22**, 403–410 (2004). doi: 10.1038/nbt955; pmid: 15060556
38. E. Seydoux *et al*., Analysis of a SARS-CoV-2-infected individual reveals development of potent neutralizing antibodies with limited somatic mutation. *Immunity* **53**, 98–105.e5 (2020). doi: 10.1016/j.immuni.2020.06.001; pmid: 32561270
39. C. Wang *et al*., A human monoclonal antibody blocking SARS-CoV-2 infection. *Nat. Commun.* **11**, 2251 (2020). doi: 10.1038/s41467-020-16256-y; pmid: 32366817
40. M. A. Tortorici *et al*., Ultrapotent human antibodies protect against SARS-CoV-2 challenge via multiple mechanisms. *Science* **370**, 950–957 (2020). doi: 10.1126/science.abe3354; pmid: 32972994
41. L. Piccoli *et al*., Mapping neutralizing and immunodominant sites on the SARS-CoV-2 spike receptor-binding domain by structure-guided high-resolution serology. *Cell* **183**, 1024–1042.e21 (2020). doi: 10.1016/j.cell.2020.09.037; pmid: 32991844
42. D. Pinto *et al*., Cross-neutralization of SARS-CoV-2 by a human monoclonal SARS-CoV antibody. *Nature* **583**, 290–295 (2020). doi: 10.1038/s41586-020-2349-y; pmid: 32422645
43. A. C. Walls *et al*., Structure, function, and antigenicity of the SARS-CoV-2 spike glycoprotein. *Cell* **181**, 281–292.e6 (2020). doi: 10.1016/j.cell.2020.02.058; pmid: 32155444
44. E. Hiramoto *et al*., The IgM pentamer is an asymmetric pentagon with an open groove that binds the AIM protein. *Sci. Adv.* **4**, eaau1199 (2018). doi: 10.1126/sciadv.aau1199; pmid: 30324136
45. D. Ugurlar *et al*., Structures of C1-IgG1 provide insights into how danger pattern recognition activates complement. *Science* **359**, 794–797 (2018). doi: 10.1126/science.aao4988; pmid: 29449492
46. E. E. Idusogie *et al*., Mapping of the C1q binding site on rituxan, a chimeric antibody with a human IgG1 Fc. *J. Immunol.* **164**, 4178–4184 (2000). doi: 10.4049/jimmunol.164.8.4178 pmid: 10754313
47. F. DiMaio *et al*., Improved low-resolution crystallographic refinement with Phenix and Rosetta. *Nat. Methods* **10**, 1102–1104 (2013). doi: 10.1038/nmeth.2648; pmid: 24076763
48. E. T. Boder, K. D. Wittrup, Optimal screening of surface-displayed polypeptide libraries. *Biotechnol. Prog.* **14**, 55–62 (1998). doi: 10.1021/bp970144q; pmid: 10858036
49. F. W. Studier, Protein production by auto-induction in high density shaking cultures. *Protein Expr. Purif.* **41**, 207–234 (2005). doi: 10.1016/j.pep.2005.01.016; pmid: 15915565
50. W. Sheffler, U. Nattermann, willsheffler/worms: Release for Science 2021, Version 1.0.1, Zenodo (2021); http://doi.org/10.5281/zenodo.4441201.
51. R. Divine, Data and design models for "Designed proteins assemble antibodies into modular nanocages," Version 1, Zenodo (2021); http://doi.org/10.5281/zenodo.4599680.
52. J. K. Leman *et al*., Macromolecular modeling and design in Rosetta: Recent methods and frameworks. *Nat. Methods* **17**, 665–680 (2020). doi: 10.1038/s41592-020-0848-2; pmid: 32483333
53. D. H. Barouch *et al*., A human T-cell leukemia virus type 1 regulatory element enhances the immunogenicity of human immunodeficiency virus type 1 DNA vaccines in mice and nonhuman primates. *J. Virol.* **79**, 8828–8834 (2005). doi: 10.1128/JVI.79.14.8828-8834.2005; pmid: 15994776
54. D. Corti *et al*., Cross-neutralization of four paramyxoviruses by a human monoclonal antibody. *Nature* **501**, 439–443 (2013). doi: 10.1038/nature12442; pmid: 23955151
55. P. B. Moore, Small-angle scattering. Information content and error analysis. *J. Appl. Cryst.* **13**, 168–175 (1980). doi: 10.1107/S002188988001179X
56. C. Suloway *et al*., Automated molecular microscopy: The new Leginon system. *J. Struct. Biol.* **151**, 41–60 (2005). doi: 10.1016/j.jsb.2005.03.010; pmid: 15890530
57. G. C. Lander *et al*., Appion: An integrated, database-driven pipeline to facilitate EM image processing. *J. Struct. Biol.* **166**, 95–102 (2009). doi: 10.1016/j.jsb.2009.01.002; pmid: 19263523
58. T. Grant, A. Rohou, N. Grigorieff, *cis*TEM, user-friendly software for single-particle image processing. *eLife* **7**, e35383 (2018). doi: 10.7554/eLife.35383; pmid: 29513216
59. K. Zhang, Gctf: Real-time CTF determination and correction. *J. Struct. Biol.* **193**, 1–12 (2016). doi: 10.1016/j.jsb.2015.11.003; pmid: 26592709
60. A. Punjani, J. L. Rubinstein, D. J. Fleet, M. A. Brubaker, cryoSPARC: Algorithms for rapid unsupervised cryo-EM structure determination. *Nat. Methods* **14**, 290–296 (2017). doi: 10.1038/nmeth.4169; pmid: 28165473
61. D. Tegunov, P. Cramer, Real-time cryo-electron microscopy data preprocessing with Warp. *Nat. Methods* **16**, 1146–1152 (2019). doi: 10.1038/s41592-019-0580-y; pmid: 31591575
62. S. H. W. Scheres, S. Chen, Prevention of overfitting in cryo-EM structure determination. *Nat. Methods* **9**, 853–854 (2012). doi: 10.1038/nmeth.2115; pmid: 22842542
63. P. B. Rosenthal, R. Henderson, Optimal determination of particle orientation, absolute hand, and contrast loss in single-particle electron cryomicroscopy. *J. Mol. Biol.* **333**, 721–745 (2003). doi: 10.1016/j.jmb.2003.07.013; pmid: 14568533
64. S. Chen *et al*., High-resolution noise substitution to measure overfitting and validate resolution in 3D structure determination by single particle electron cryomicroscopy. *Ultramicroscopy* **135**, 24–35 (2013). doi: 10.1016/j.ultramic.2013.06.004; pmid: 23872039
65. J. Mathieu *et al*., HIF induces human embryonic stem cell markers in cancer cells. *Cancer Res.* **71**, 4640–4652 (2011). doi: 10.1158/0008-5472.CAN-10-3320; pmid: 21712410
66. K. L. DeCicco-Skinner *et al*., Endothelial cell tube formation assay for the in vitro study of angiogenesis. *J. Vis. Exp.* **2014**, e51312 (2014). doi: 10.3791/51312; pmid: 25225985
67. K. H. D. Crawford *et al*., Protocol and reagents for pseudotyping lentiviral particles with SARS-CoV-2 spike protein for neutralization assays. *Viruses* **12**, 513 (2020). doi: 10.3390/v12050513; pmid: 32384820

ACKNOWLEDGMENTS

We thank Y. Hsia and R. Mout for help with computational design and B. Fiala, N. Brunette, E.Kepl, M. DeWitt, L. Carter, M. Murphy, and C. Correnti for providing protein materials used at various stages of the project; A. Courbet for help collecting micrographs for d3.08 and d3.36 designs and J. Quipse for help maintaining and operating the electron microscopes used; O. Poncelet for technical help; Amgen for the AMG-655 antibody; S. Akilesh for providing the primary kidney tubular epithelial cells; and W. Kaelin for providing the RCC4 cell line. The SAXS work was conducted at the Advanced Light Source (ALS), a national user facility operated by Lawrence Berkeley National Laboratory on behalf of the Department of Energy (DOE), Office of Basic Energy Sciences, through DOE BER IDAT grant (DE-AC02-05CH11231) and NIGMS-supported ALS-ENABLE (GM124169-01) and National Institute of Health project MINOS (R01GM105404). We thank the staff at the Advanced Light Source SIBYLS beamline at Lawrence Berkeley National Laboratory, including K. Burnett, G. Hura, M. Hammel, J. Tanamachi, and J. Tainer for the services provided through the mail-in SAXS program, which is supported by the DOE Office of Biological and Environmental Research Integrated Diffraction Analysis program DOE BER IDAT grant DE-AC02-05CH11231 and NIGMS-supported ALS-ENABLE (GM124169-01) and National Institute of Health project MINOS (R01GM105404). **Funding:** This work was supported by NSF grant CHE 1629214 (N.P.K. and D.B.), HHMI (W.S. and D.B), the Audacious Project at the Institute for Protein Design (R.D., I.V., M.R.T., and A.R.), the Washington Research Foundation (F.S. and J.L.), the Nordstrom-Barrier Directors Fund at the Institute for Protein Design (A.E.), Washington State General Operating Fund for the Institute for Protein Design (L.Ste.), Wu Tsai Translational Investigator Fund (G.U.), Nan Fung Life Sciences Translational Investigator Fund (J.A.F.), NIH/NIDCR grant T90 DE021984 and NIH/NCATS TR002318 (Y.T.Z.), donations to Fred Hutch COVID-19 Research Fund (M.F.J., L.J.H., Y.-H.W., A.T.M., and L.Sta.), NIH grant R01AI127726 (P.A.M., M.L.F., and D.J.C.), NIH/NCI Cancer Center Support Grant P30 CA015704 and ISCRM Pilot Award for J.M., NIAID/NIH (DP1AI158186 and HHSN272201700059C to D.V.), NIGMS/NIH (R01GM120553 to D.V.), a Pew Biomedical Scholars Award to D.V., and a Burroughs Wellcome Investigators in the Pathogenesis of Infectious Diseases award to D.V., Fast Grants (D.V.), the University of Washington Arnold and Mabel Beckman cryoEM center. **Author contributions:** R.D., H.V.D., G.U., J.A.F., J.M., D.V., and D.B. designed the research. R.D. designed the AbC-forming oligomers with contributions from I.V. and D.B. for d2.3, d2.4, d2.7, and t32.4. I.V., W.S., and D.B. wrote the computational fusion protocol used during design, based on I.V.'s original concept. R.D., H.V.D., G.U., J.A.F., and A.R. produced and characterized all designs. F.S. designed and characterized the Fc-binding repeat protein. R.D. and A.E. prepared samples for SAXS analysis, and R.D., G.U., J.A.F., and A.E. analyzed the SAXS results. R.D. and H.V.D. prepared the NS-EM grids. H.V.D., R.D., and A.E. collected NS-EM data. R.D. analyzed the NS-EM datasets. H.V.D. prepared samples and analyzed the cryo-EM datasets for o42.1 and i52.3 nanocages with Fc. A.E., G.U., J.A.F., M.M., and R.D. designed and characterized d3.08 and d3.36. R.D. and J.L. designed and conducted the stability and exchange experiments. G.U., J.A.F., S.S., J.L., H.R.-B., and J.M. designed the DR5 experiments, with S.S. performing the assays. G.U., J.A.F., Y.T.Z., I.X.R., J.M., and H.R.-B. designed the A1F-Fc experiments, with Y.T.Z. and I.X.R. performing the assays. M.R.T., R.D., N.P.K., and D.B. designed the CD40 agonist experiments, with M.R.T. conducting the cell culture assays. P.A.M., M.L.F., and D.J.C. designed and conducted the T cell proliferation assays. M.F.J., L.J.H., Y.-H.W., A.T.M., and L.Sta. designed the pseudovirus neutralization studies with IgGs. H.V.D., A.C.W., L.Ste., D.V., and D.B. designed the pseudovirus neutralization studies with Fc-ACE2. **Competing interests:** R.D., I.V., W.S., F.S., and D.B. are inventors on U.S. provisional patent application no. 63/085,351 filed by the University of Washington on the AbC-forming design

sequences. R.D., G.U., J.A.F., J.L., M.R.T., N.P.K., J.M., and D.B. are inventors on U.S. provisional patent application no. 63/088,576 filed by the University of Washington on the DR5 and CD40 AbC applications. R.D., G.U., J.A.F., J.L., Y.T.Z., H.R.-B., and D.B. are inventors on U.S. provisional patent application no. 63/088,576 filed by the University of Washington on the A1F-Fc AbC applications. A.T.M. and L.Sta. are inventors on U.S. provisional patent application no. 63/016268 filed by the Fred Hutchinson Cancer Research Center on the SARS-CoV-2–specific monoclonal antibodies discussed here. R.D., L.Ste., L.Sta., and D.B. are inventors on U.S. provisional patent application no. 63/088,576 filed by the University of Washington covering the CoV-2 S AbC applications. N.P.K. is a cofounder, shareholder, paid consultant, and chair of the scientific advisory board of Icosavax, Inc., and has received an unrelated sponsored research agreement from Pfizer. D.V. is a consultant for Vir Biotechnology, Inc. The Veesler laboratory has received an unrelated sponsored research agreement from Vir Biotechnology, Inc. The other authors declare no competing interests. **Data and materials availability:** 3D maps from EM have been uploaded to the Electron Microscopy Data Bank (EMDB) with accession numbers EMD-23266 (o42.1 Fc) and EMD-23265 (i52.3 Fc). WORMS code is available in Zenodo (*50*). Design models, building blocks, symmetry definition files, and example scripts for making fusions and designing fusion outputs can also be found in Zenodo (*51*). All other data are available in the manuscript or supplementary materials.

SUPPLEMENTARY MATERIALS

science.sciencemag.org/content/372/6537/eabd9994/suppl/DC1
Figs. S1 to S11
Tables S1 to S15
References
MDAR Reproducibility Checklist
Data S1 to S6

View/request a protocol for this paper from *Bio-protocol*.

24 July 2020; resubmitted 23 November 2020
Accepted 10 February 2021
10.1126/science.abd9994